



“One stone four birds” design atom co-sharing BiOBr/Bi₂S₃ S-scheme heterojunction photothermal synergistic enhanced full-spectrum photocatalytic activity

Junhao Ma^a, Liang Xu^a, Zhaoyi Yin^a, Zhifeng Li^a, Xiaoyi Dong^a, Zhiguo Song^a, Daomei Chen^{b,*}, Rui Hu^{c,d}, Qi Wang^a, Jin Han^a, Zhengwen Yang^a, Jianbei Qiu^a, Yongjin Li^{a,*}

^a Faculty of Materials Science and Engineering, Kunming University of Science and Technology, Kunming 650093, China

^b National Center for International Research on Photoelectric and Energy Materials, School of Materials and Energy, Yunnan University, Kunming 650091, China

^c College of Chemistry and Chemical Engineering, China West Normal University, Nanchong 637000, China

^d Key Laboratories of Fine Chemicals and Surfactants in Sichuan Provincial Universities, Sichuan University of Science and Engineering, Zigong 643000, China

ARTICLE INFO

Keywords:

BiOBr/Bi₂S₃

S-scheme heterojunctions

Atom co-sharing

Photothermal effect

Full-spectrum-light photocatalytic activities

ABSTRACT

The rational design of heterostructure photocatalysts holds significant scientific and technical importance for maximizing the utilization of solar energy. In this study, a full spectrum-responsive S-scheme BiOBr/Bi₂S₃ heterojunction with co-sharing Bi atoms had been successfully constructed using an ion exchange approach accompanied by an in-situ growth process. Theoretical calculations and advanced techniques analysis demonstrate that the interfacial co-sharing of Bi atoms and the internal electric field (IEF) between BiOBr and Bi₂S₃ can greatly enhance S-scheme charge transfer, leading to effective spatial charge separation and the maintenance of maximum redox capacity. Additionally, the incorporation of Bi₂S₃ and the formation of oxygen vacancies (OVs) significantly increased NIR absorption and enhanced the photothermal property, further improving charge separation and utilization. As a result, the optimal photoreduction of Cr(VI) performance in BiOBr/Bi₂S₃ reached 100% within 10 min of full-spectrum light irradiation, and the CO yield was 20.32 μmol·g⁻¹ after 5 h of irradiation, which were 31.97 and 3.07 times higher than those of BiOBr, respectively. Furthermore, we elucidated the mechanism of Cr(VI) removal using DFT. This work provides valuable guidance for the rational design and construction of Bi-based S-scheme heterojunction photocatalysts with high-efficiency photocatalytic performance and effective solar light utilization.

1. Introduction

Energy crises and environmental pollution represent two major challenges confronting the sustainable development of society [1–3]. Sunlight-driven photocatalysis has long been considered one of the most promising pathways for achieving solar-to-chemical energy conversion, finding widespread application in areas such as pollutant degradation, water splitting, CO₂ reduction, NO removal, and solar cell technology, among others [4–8]. Unfortunately, the practical application of this technology has been hindered significantly by inefficient solar energy utilization, primarily due to low light capture capabilities and the rapid accumulation of photogenerated carriers [9,10]. Currently, most photocatalysts can only capture ultraviolet (UV) and visible (Vis) light for photocatalytic reactions, neglecting the potential of near-infrared (NIR)

light, which accounts for over 50% of solar radiation and has been overlooked due to its low photon energy, making it challenging to directly activate photocatalysts for chemical reactions [11]. However, NIR light can increase the reaction system's temperature through photothermal effects, which benefit photocatalytic reactions [12]. Effectively harnessing NIR light to improve solar energy conversion efficiency and enhance photocatalytic performance is of great significance. Currently, it is a challenge for a single-component photocatalyst to simultaneously possess a broad light absorption range and strong redox ability. Furthermore, the low efficiency of photogenerated carrier separation and transfer presents another obstacle in practical applications, resulting in suboptimal solar energy utilization.

Encouragingly, the creation of S-scheme heterojunctions is regarded as a promising solution to address these challenges by improving the

* Corresponding authors.

E-mail addresses: dmchen@ynu.edu.cn (D. Chen), liyongjin@kust.edu.cn (Y. Li).

<https://doi.org/10.1016/j.apcatb.2023.123601>

Received 26 September 2023; Received in revised form 9 November 2023; Accepted 13 December 2023

Available online 19 December 2023

0926-3373/© 2023 Elsevier B.V. All rights reserved.

separation efficiency of photogenerated carriers and enhancing the redox abilities of electrons (e^-) and holes (h^+) [13]. An S-scheme heterojunction consists of a reduction photocatalyst (RP) with a higher conduction band (CB) level and Fermi level and an oxidation photocatalyst (OP) with a lower valence band (VB) level and Fermi level. When they come into contact, electrons are transferred from RP to OP due to differences in Fermi energy levels, creating an internal electric field (IEF) directed from RP to OP at their interface and causing the energy band edge to bend. This IEF and energy band bending combination prevents the recombination of photogenerated electrons in the CB of OP and holes in the VB of RP while retaining photogenerated e^- and h^+ with strong redox capacity. Thus, the S-scheme heterojunction not only enhances the separation and migration of carriers but also preserves their strong redox ability. Additionally, incorporating narrower bandgap semiconductors into the heterostructure greatly expands the photocatalyst's light absorption range while maintaining efficient charge separation, leading to improved photocatalytic efficiency. Consequently, due to these excellent characteristics, S-scheme heterojunctions have found extensive applications in various photocatalytic processes, including CO_2 reduction, photocatalytic H_2 evolution, H_2O_2 production, N_2 fixation, pollutant degradation, and the reduction of harmful metal ions [5,14–19].

However, most reported S-scheme heterojunctions lack a close atomic-level interface contact, making it challenging to establish a strongly coupled interface for effective charge separation. This limitation results in lower charge transfer efficiency within the heterojunction, which in turn impacts the activities and stability of photocatalysts [20]. From a structural perspective, efficient charge separation depends not only on suitable band structures but also on intimate interfacial connections that minimize interfacial charge transfer resistance and provide more charge migration channels. This enables the successful migration of photogenerated electrons and the establishment of a strong IEF at the heterointerface. Compared to conventional heterostructures, constructing “atom-cosharing” heterostructures offers a promising approach to create heterostructures with specific atomic-level interfacial contacts. In this scenario, common atoms act as nucleation sites, bridging the two heterogeneous components together so that one component grows in situ on the surface of the other component. Additionally, this approach ensures low lattice mismatch, which is conducive to charge separation and transfer [21]. To date, atom-cosharing heterostructures have been designed and shown to improve photocatalytic performance, including examples like Cs_2SnI_6/SnS_2 [22], $SnO_2/SnSe_2$ [23], $Cs_3Bi_2I_9/Bi_2WO_6$ [21], $Cs_xWO_3/CsPbBr_3$ [24], WO_3/Bi_2WO_6 [25], $Cs_3Bi_2Br_9/Bi-MOF$ [26], and $BiVO_4 @Bi_2S_3$ [27]. These results indicate that atomic-level close contact with strong chemical bonding interactions can be achieved through atom-cosharing, thereby shortening the charge transfer distance and promoting charge separation. Therefore, constructing S-scheme heterojunctions with atomic-level contact by sharing atoms is a promising approach to building efficient and advanced photocatalytic materials.

Recently, bismuth-based semiconductor photocatalysts have gained significant attention in research due to their excellent visible light absorption performance, unique electronic structure, and high stability [28]. Specifically, BiOBr exhibits an appropriate band structure, with the valence band (VB) mainly composed of O 2p and Br 4p orbitals, giving BiOBr strong oxidation capacity [29]. Moreover, it features a fluorite-like $[Bi_2O_2]^{2+}$ structure interleaved with double halogen atoms $[Br]^-$ slabs through van der Waals interactions along the [001] direction. This arrangement forms an internal electrostatic field, facilitating the separation of photogenerated carriers and contributing to high photocatalytic performance [30]. However, the original BiOBr photocatalyst's performance needs further improvement due to limited utilization of visible light ($\lambda \leq 450$ nm), rapid compounding of photogenerated carriers, and a high CB position that restricts its reduction capability. Among various bismuth-based photocatalysts, Bi_2S_3 stands out due to its layered structure and narrower band gap

(1.3–1.7 eV) [31], enabling absorption of visible and NIR light energies, leading to a broad spectral response. Additionally, Bi_2S_3 exhibits NIR light-triggered photothermal performance, which can elevate the reaction environment's temperature, enhancing photothermocatalytic degradation reactions [32]. Unfortunately, due to the speediness recombination of photogenerated carriers, the photocatalytic activity of pure Bi_2S_3 is lower. Owing to its higher CB and VB potential, Bi_2S_3 is often employed as a reduction catalyst to form heterostructures with other semiconductors, thereby enhancing photocatalytic capacity. Fortunately, given that Bi_2S_3 belongs to the same bismuth series as BiOBr and shares a proper band structure and high lattice matching, it shows great potential for forming illustrious heterojunctions. Additionally, Bi_2S_3 possesses extremely low solubility (K_{sp}) [33], making it convenient to generate Bi_2S_3 in situ on the surface of 2D BiOBr nanosheets to create an S-scheme heterojunction via ion exchange driven by S^{2-} . This ion exchange process breaks the internal Bi–O bond layered $[Bi_2O_2]^{2+}$ of BiOBr, forming oxygen vacancies (OVs) [34], while simultaneously generating Bi_2S_3 nanorods on the BiOBr nanosheet surface. The introduction of OVs benefits both charge separation and surface reactant adsorption [35]. These characteristics make BiOBr and Bi_2S_3 strong candidates for constructing atomic-shared S-scheme heterostructures. Thus far, $Bi_2S_3/BiOBr$ -based heterostructures have been reported for various photocatalytic applications, including the degradation of organic pollutants, Cr(VI) reduction, CO_2 reduction, and more [4,36]. Despite the encouraging progress in exploring $Bi_2S_3/BiOBr$ -based heterostructures, the influence of co-sharing Bi atoms providing an atomic-level interfacial channel has been overlooked. In particular, the cooperative effect of S-scheme heterojunctions and photothermal conversion on photocatalytic performance has not been thoroughly investigated.

Herein, we designed and constructed a full-spectrum-responsive BiOBr/ Bi_2S_3 S-scheme heterojunction with co-sharing Bi atoms by in-situ growing Bi_2S_3 nanorods on BiOBr nanosheets. We investigated the influence of photothermal effects in this system, which has not been explored in previous BiOBr/ Bi_2S_3 heterojunction studies. Our work systematically characterized the composition, morphology, structure, and optical response performance of BiOBr/ Bi_2S_3 heterojunctions. We validated the photocatalytic performance of S-scheme BiOBr/ Bi_2S_3 heterojunctions in reducing Cr(VI) and CO_2 . The relationship between photocatalytic activity and structure was discussed, considering light absorption, band structure, IEF at the interface, charge separation/migration, and photothermal effects, using both theoretical calculations and experimental characterizations. Additionally, we proposed and discussed the relevant mechanism.

2. Experimental

2.1. Preparation of photocatalysts

The BiOBr/ Bi_2S_3 S-scheme heterojunctions were synthesized using a straightforward ion exchange method followed by an in-situ growth process. Initially, BiOBr (2 mmol) was dissolved in 30 mL of deionized water and stirred magnetically for 30 min to ensure uniform dispersion. Subsequently, varying volumes of $Na_2S_2O_3$ solution (1 mol·L⁻¹; 0.5 mL, 1 mL, 2 mL, 3 mL) were added to the BiOBr suspension and stirred magnetically for an additional 30 min. Finally, the suspension was transferred into a 50 mL Teflon-lined autoclave and heated to 180 °C for 6 h. After the reaction, the autoclave was allowed to cool naturally. The resulting products were collected and separated through centrifugation, washed with ethanol and deionized water several times, and then dried at 70 °C in ambient air. The preparation methods of BiOBr and Bi_2S_3 were described in the [Supporting material](#).

2.2. Characterization

A series of Basic material characterizations were provided in the

Supporting material.

2.3. Photocatalytic and photothermocatalytic performance

The photocatalytic performance of BiOBr/Bi₂S₃ heterojunction was tested by using different filters under Vis-NIR light ($420\text{ nm} \leq \lambda \leq 2000\text{ nm}$), NIR light ($800\text{ nm} \leq \lambda \leq 2000\text{ nm}$), full-spectrum light ($300\text{ nm} \leq \lambda \leq 2000\text{ nm}$) with a 300 W Xe lamp. Typically, 20 mg photocatalysts was placed in 40 mL Cr(VI) solution ($10\text{ mg}\cdot\text{L}^{-1}$). The suspension was equilibrated in the dark for 2 h to reach adsorption-desorption equilibrium, then 3.5 mL suspension was removed at regular intervals after sunlight irradiation, and the supernatant was tested by the diphenylcarbazide (DPC) method after centrifugation. In the photothermocatalytic experiment, Temperature regulation of the catalytic environment using a thermostatic magnetic stirring heating jacket and water circulation. The photocatalytic performance under different single band illumination was evaluated by Merry Change LED multi-bit photochemical reaction instrument, and the test means were the same

as above.

2.4. Theoretical calculations

The Theoretical calculations (DFT) were provided in the [Supporting material](#).

3. Results and discussion

3.1. Structural characterization and surface properties

The BiOBr/Bi₂S₃ S-scheme heterojunctions were synthesized through a simple ion exchange method, followed by an in-situ growth process, as depicted in Fig. 1a. Initially, the BiOBr nanosheets precursor was prepared using a solvothermal method. Subsequently, the BiOBr/Bi₂S₃ heterojunction was formed through an in-situ ion exchange method by dispersing BiOBr nanosheets in a solution containing the S source (Na₂S₂O₃) (refer to the Experimental section for details). Here,

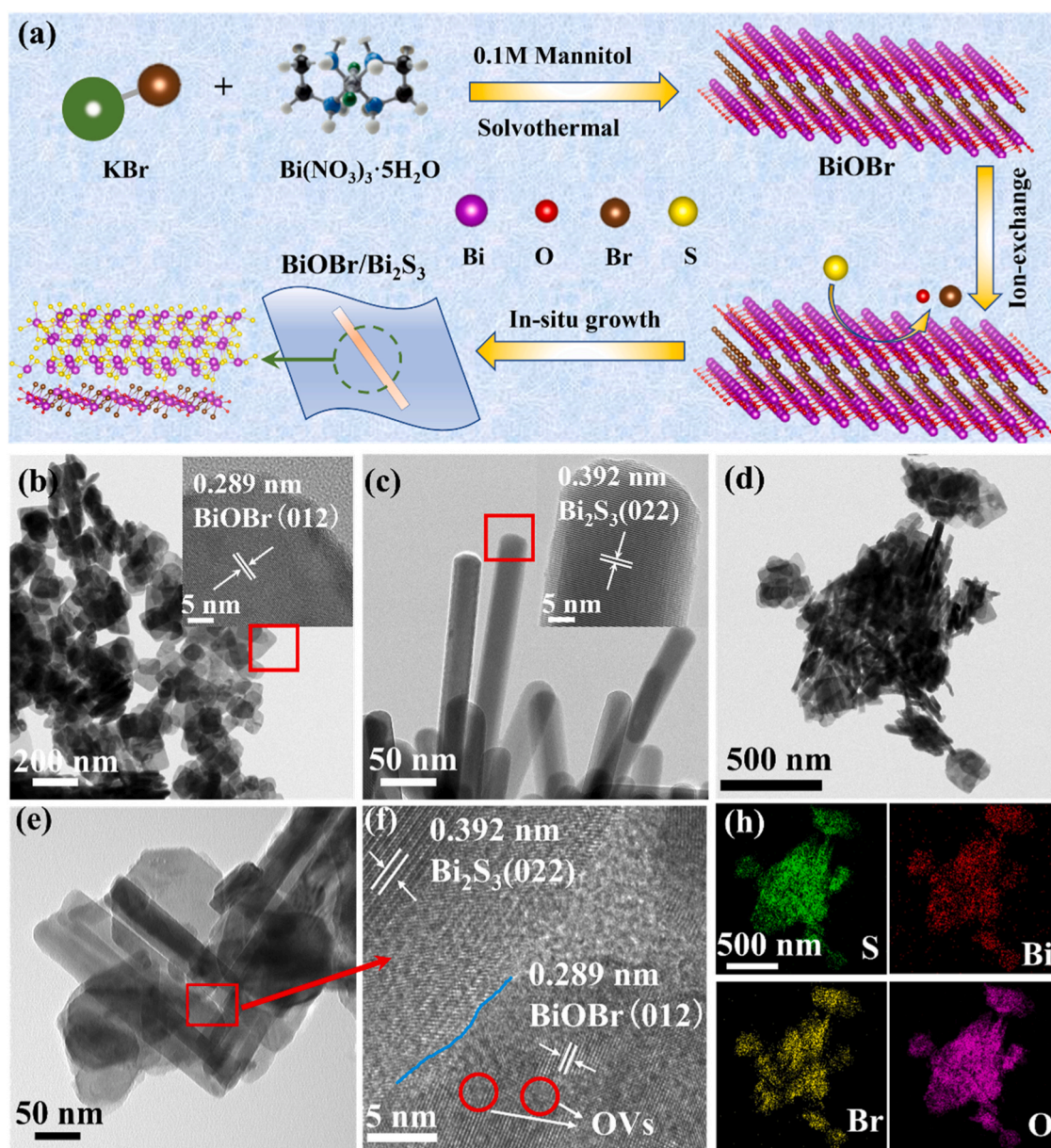


Fig. 1. (a) Schematic diagram illustrating the synthesis of the BiOBr/Bi₂S₃ heterostructure; TEM and HRTEM images of (b) BiOBr, (c) Bi₂S₃, and (e, f) B-2S; (d) TEM and (h) EDX elemental mapping images of B-2S.

the S source was controlled at 0.5, 1, 2, or 3 mmol, resulting in the corresponding products designated as B-0.5S, B-1S, B-2S, and B-3S, respectively. In contrast to traditional monomer recombination methods, the in-situ ion exchange method facilitates the construction of a closely contacting interface between the two materials, serving as a pathway for the rapid transfer of carriers and thereby enhancing photocatalytic efficiency.

The morphologies of the as-prepared BiOBr, Bi₂S₃, and BiOBr/Bi₂S₃ heterojunctions were examined using scanning electron microscopy (SEM). BiOBr exhibited a 2D nanosheet morphology with an average size of approximately 100 nm (Fig. S1a). This unique 2D morphology not only reduces the diffusion length of photogenerated carriers but also provides a large surface area for the deposition of Bi₂S₃. Bi₂S₃ displayed a nanorod morphology with a diameter of 30 nm (Fig. S1b). Upon reacting with S in a hydrothermal environment, the morphology of BiOBr nanosheets changed significantly, indicating the occurrence of an ion exchange reaction leading to the formation of a composite (Fig. S1c-f). It is evident that the density of Bi₂S₃ nanorods grown on the BiOBr nanosheets increased with higher S concentrations. Typically, Bi₂S₃ crystals tend to grow along the [001] direction, resulting in a rod-like structure [37]. Therefore, the nanorods observed on the surface of BiOBr nanosheets are presumed to be Bi₂S₃. In the hydrothermal environment, Na₂S₂O₃ releases S²⁻ into the reaction solution which then reacts with BiOBr, as the K_{sp} of Bi₂S₃ is lower than that of BiOBr (BiOBr: 3.0×10^{-7} , Bi₂S₃: 1.0×10^{-97}) [33,38]. The ion exchange reaction is represented as $2\text{BiOBr} + 3\text{S}^{2-} + 2\text{H}_2\text{O} \rightarrow \text{Bi}_2\text{S}_3\downarrow + 2\text{Br}^- + 4\text{OH}^-$. Consequently, S²⁻ reacts with Br⁻ from the outermost surface of BiOBr to the interior over time, ultimately forming an optimized BiOBr/Bi₂S₃ heterojunction structure through the co-sharing of Bi atoms.

Transmission electron microscope (TEM) analysis further examined the morphology and microstructure. The TEM image of BiOBr revealed a typical flake-like morphology (Fig. 1b), consistent with the SEM results. The lattice fringe spacing of 0.289 nm observed in the corresponding HRTEM images was attributed to the (012) crystal plane of BiOBr. TEM images in Fig. 1c further confirmed the nanorod structure of pure Bi₂S₃ with a diameter of 30 nm, and the HRTEM image displayed a lattice fringe spacing of 0.392 nm, corresponding to its (022) crystal plane. The

TEM images of the synthesized B-2S heterojunctions in Fig. 1d and e clearly showed that Bi₂S₃ nanorods closely adhered to the BiOBr nanosheets, confirming their close contact and aligning with the SEM observations. This unique 2D/1D heterojunction promotes high-quality interfacial contacts and maximizes the exposure of reaction sites, enhancing photocatalytic activity [39]. Additionally, HRTEM analysis (Fig. 1f) of B-2S further elucidated the contact between the two materials, with an evident contact interface (indicated by the blue line) and distinct lattice fringes. The lattice fringe spacings of 0.289 nm and 0.392 nm corresponded to the (012) planes of tetragonal phase BiOBr and the (022) crystal plane of orthorhombic phase Bi₂S₃, respectively. Furthermore, discontinuous lattice fringes indicated the possible presence of OV in B-2S. The HRTEM results demonstrated that Bi₂S₃ could be directly grown on and attached to the BiOBr nanosheets. Energy-dispersive X-ray (EDX) elemental mapping (Fig. 1h) revealed the uniform distribution of S, Bi, Br, and O elements in the B-2S heterojunction. Since no additional Bi precursor was introduced during the reaction, the Bi atoms on the surface of BiOBr served as both the source for Bi₂S₃ and the growth site for Bi₂S₃. Therefore, BiOBr and Bi₂S₃ could establish a close contact through the co-sharing of Bi atoms. These results validated the successful synthesis of the BiOBr/Bi₂S₃ heterojunction with a co-sharing Bi atoms contact interface, facilitating the rapid transfer of photogenerated e⁻-h⁺ pairs.

The phase compositions and crystal structures of the synthesized samples were examined using X-ray diffraction (XRD) measurements. As shown in Fig. 2a, the diffraction peaks of pristine BiOBr and Bi₂S₃ matched the characteristic peaks of standard tetragonal BiOBr (JCPDS: 73-2061) and orthorhombic Bi₂S₃ (JCPDS: 84-0279), respectively. As expected, the prepared BiOBr/Bi₂S₃ heterojunctions exhibited characteristic peaks of both BiOBr and Bi₂S₃, without any impurities detected. Notably, the low-intensity peaks at $2\theta = 25.0^\circ$ and 28.6° corresponding to (111) and (121) planes of Bi₂S₃ became more prominent with an increased proportion of Bi₂S₃ in the heterojunction, confirming the successful preparation of the heterojunction. Furthermore, to assess the co-sharing of Bi atoms, a mismatching factor was calculated. As depicted in Fig. S2, the vertical distance between adjacent Bi planes in BiOBr (3.915 Å) is similar to that in Bi₂S₃ (3.981 Å), resulting in a low

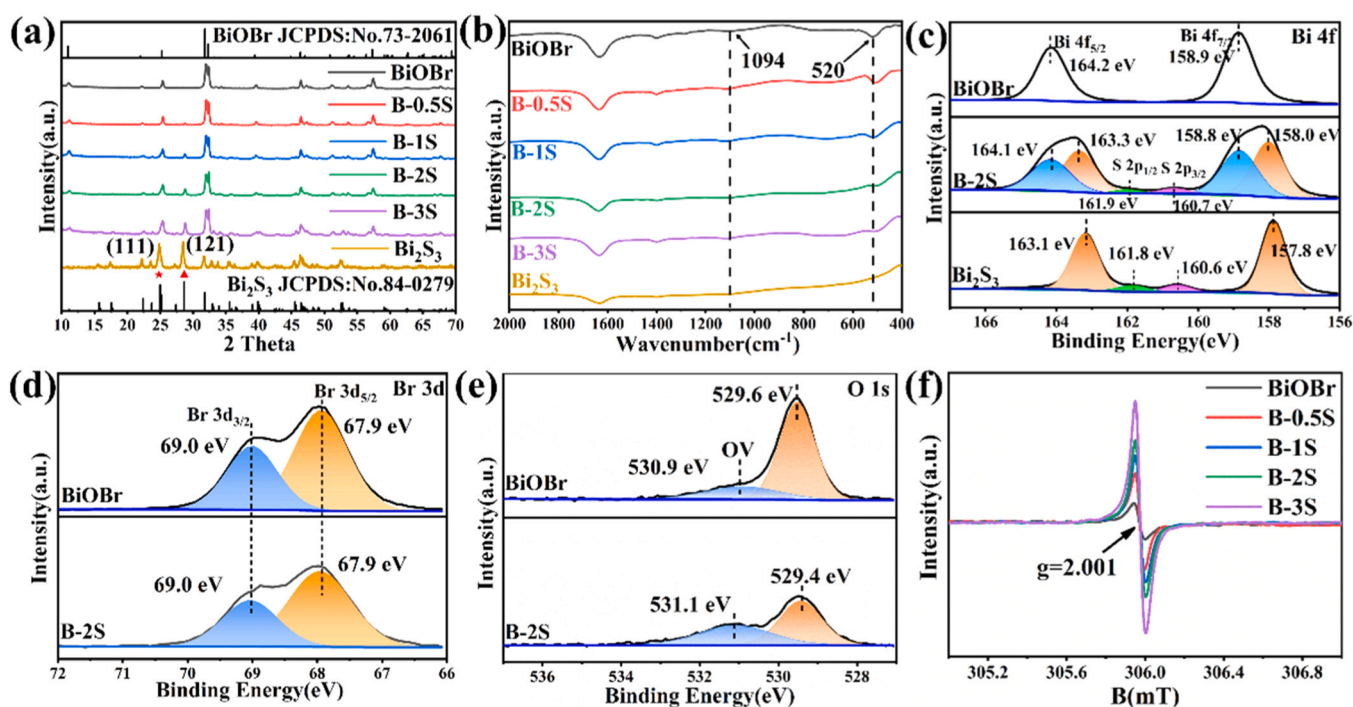


Fig. 2. (a) XRD patterns and (b) FTIR spectra of the BiOBr/Bi₂S₃ heterojunction. XPS spectra of as-prepared samples: (c) Bi 4f, (d) Br 3d, (e) O 1s; (f) EPR spectra of the BiOBr/Bi₂S₃ heterojunction at room temperature.

mismatch factor (f) of 1.6% [$f = |1 - d(\text{Bi}_2\text{S}_3)/d(\text{BiOBr})| \times 100\%$], where d represents the vertical distance between adjacent Bi planes in the BiOBr [100]|| Bi_2S_3 [100] direction [22]. This low mismatch indicates favorable matching energy between the two planes, providing suitable conditions for embedding Bi_2S_3 in the BiOBr crystal lattice and epitaxial crystal growth.

Subsequently, the chemical bonding between BiOBr and Bi_2S_3 was confirmed through FTIR spectroscopy. In all samples, characteristic peaks at 3447 cm^{-1} and 1626 cm^{-1} were observed, originating from hydroxyl groups on the sample surface and the characteristic bending vibration peak of free water in the sample (Fig. S3a) [40]. The characteristic FTIR spectrum of BiOBr displayed peaks at 520 cm^{-1} (Fig. 2b), attributed to the vibrations of Bi–O single bonds [41]. For Bi_2S_3 , the characteristic peak at 1094 cm^{-1} corresponded to the tensile vibration of Bi–S bonds [42]. In the BiOBr/ Bi_2S_3 heterojunction, the vibrational peak intensity of the Bi–S bond slightly increased with higher Bi_2S_3 loading, while the peak intensities of Bi–O significantly decreased. Simultaneously, the peaks shifted towards higher wavenumbers, indicating chemical interaction between BiOBr and Bi_2S_3 [43], suggesting the formation of O–Bi–S bonds between them, further confirming the co-sharing of Bi atoms.

The chemical states and interfacial interactions of the BiOBr/ Bi_2S_3 heterojunctions were thoroughly investigated using X-ray photoelectron spectroscopy (XPS) (Fig. S3b). The survey XPS spectrum confirmed the presence of Bi, O, Br, and S elements, consistent with the results of EDS mapping. Fig. 2c presents the high-resolution XPS of Bi 4f for pristine BiOBr, Bi_2S_3 , and B-2S. Interestingly, the binding energy of Bi in BiOBr and Bi_2S_3 differed significantly, indicating distinct chemical coordination environments. For B-2S, the peaks at 158.8 and 164.1 eV were assigned to Bi 4f_{7/2} and Bi 4f_{5/2}, respectively, corresponding to Bi^{3+} ions in BiOBr [44], whereas peaks near 158.0 and 163.3 eV were attributed to Bi_2S_3 . Additionally, weak double peaks near 160.7 and 161.9 eV belonged to S 2p_{3/2} and S 2p_{1/2}, affirming the presence of S^{2-} [5]. Significantly, compared to BiOBr and Bi_2S_3 , the BiOBr–Bi 4f in B-2S exhibited a slight shift towards lower binding energies, while the Bi_2S_3 –Bi 4f showed a higher-energy shift, indicating that the interface contact occurred through the Bi element. Furthermore, the S 2p peak in B-2S shifted towards higher binding energy. These results indicated electron transfer between BiOBr and Bi_2S_3 upon their combination. In Fig. 2d, the two peaks at 68.0 and 69.1 eV in the Br 3d spectra of BiOBr and B-2S pertained to Br 3d_{5/2} and Br 3d_{3/2}, respectively. The binding energy remained unchanged between BiOBr and B-2S, suggesting that interface contact did not involve Br. Fig. 2e revealed two splitting peaks near 529.6 eV and 530.9 eV in BiOBr, corresponding to lattice oxygen (Bi–O) and oxygen vacancies (OVs) [42]. Clearly, the peak intensities of lattice oxygen (Bi–O) in B-2S were reduced compared to pure BiOBr, possibly due to the O–Bi–S bond at the interface, resulting in a decreased amount of chemisorbed oxygen [45]. Concurrently, lattice oxygen (Bi–O) shifted towards lower binding energy, further confirming charge transfer at the interface between BiOBr and Bi_2S_3 . Typically, binding energy increases with decreasing electron density, while binding energy decreases with increasing electron density [14]. Therefore, these results strongly support the transfer of electrons from Bi_2S_3 to BiOBr in the BiOBr/ Bi_2S_3 heterojunction, facilitated by the co-sharing of Bi atoms and strong chemical interaction between the two materials. This electron transfer leads to the formation of an IEF at the interface in the Bi_2S_3 to BiOBr direction, promoting the creation of the S-scheme BiOBr/ Bi_2S_3 heterojunction.

In addition, it can be clearly seen that the peak intensity of OVs in B-2S is much higher than that in the original BiOBr. This indicates a significant increase in the content of OVs. The EPR spectrum verifies this result (Fig. 2f), as B-3S exhibits the strongest OVs signal ($g = 2.001$) [46]. These results confirm that the defects in the BiOBr/ Bi_2S_3 heterojunction are caused by OVs, which can be attributed to the ion-exchange process between BiOBr and $\text{Na}_2\text{S}_2\text{O}_3$. This process leads to the in-situ replacement of Br^- and O_2^- in BiOBr by S^{2-} . Consequently, under high

temperature, the internal Bi–O bond within the $[\text{Bi}_2\text{O}_2]^{2+}$ layers of BiOBr are disrupted, resulting in the generation of more OVs on the heterostructure's surface [5]. The formation of a large number of OVs can expand the optical responsive region, enhance the separation of photogenerated e^- – h^+ pairs, and boost the adsorption of surface reactants. This results in a significant improvement in photocatalytic ability. Based on these characterizations, we can conclude that the BiOBr/ Bi_2S_3 heterojunction with interfacial OVs was successfully prepared via an ion exchange approach accompanied by an in-situ growth strategy.

3.2. Optical absorption properties and photothermal effect

Traditionally, the lower utilization rate of photocatalysts for solar energy significantly restricts the development of photocatalysis technology. Expanding the light absorption range is conducive to enhancing the activity of photocatalytic materials. Therefore, the photoabsorption properties of the as-synthesized BiOBr/ Bi_2S_3 heterostructures were examined using UV-Vis-NIR diffuse reflectance spectroscopy. The pure BiOBr and Bi_2S_3 exhibited characteristic absorption edges at 450 nm and 1300 nm, respectively (Fig. 3a). This indicates the Vis and UV-Vis-NIR light-responsive behavior of BiOBr and Bi_2S_3 , respectively, in line with previous reports [36]. Notably, after loading Bi_2S_3 , the optical absorption of BiOBr/ Bi_2S_3 is substantially extended into the NIR region ($>1000\text{ nm}$), and the absorption intensity significantly improved with the increase of Bi_2S_3 content, resulting in a change in color from white to black (Fig. S4). This implies that the material has latent photothermal properties. Excitingly, compared to pure Bi_2S_3 , a strong NIR absorption peak of the BiOBr/ Bi_2S_3 heterojunction between 1000 and 1800 nm was observed. This may be caused by the localized surface plasmon resonance (LSPR) effect of OVs, which could enhance the photothermal performance [47]. Thanks to this expanded light absorption range (200–1800 nm) and intensity, the BiOBr/ Bi_2S_3 heterojunction is expected to enhance the efficiency of solar energy utilization and photothermal conversion, thereby significantly enhancing photocatalytic activity. The improved light absorption ability of the composites is advantageous for increasing photocatalytic activity.

The photothermal effect plays a crucial role in enhancing photocatalytic activity [48]. Generally, the surface temperature of the photocatalyst can directly reflect its photothermal conversion ability. For this purpose, the surface temperature changes of BiOBr, B-2S, and Bi_2S_3 samples were measured using an infrared (IR) camera under Xenon lamp irradiation. As shown in Fig. S5, the surface temperatures of BiOBr, B-2S, and Bi_2S_3 rose to 79.6°C , 131.0°C , and 95.1°C , respectively, after 60 s of full-spectrum irradiation. Noticeably, both B-2S and Bi_2S_3 could still reach 75.3°C and 63.5°C , respectively, under NIR light irradiation at $\lambda = 850\text{ nm}$ (Fig. 3b and c). Significant temperature increases were also observed under visible light ($420 \leq \lambda \leq 780\text{ nm}$) irradiation (Fig. S7), whereas there were no significant temperature changes under UV light ($300 \leq \lambda \leq 400\text{ nm}$) irradiation (Fig. S8). This implies that most of the heat is generated by low-frequency NIR photons [49]. Furthermore, the sample temperature dropped rapidly when the light was turned off (Fig. 3d). These results show that B-2S and Bi_2S_3 both exhibit excellent photothermal performance due to their NIR absorption capacity, which allows them to convert light energy into thermal energy. Interestingly, when compared to the pure Bi_2S_3 sample, B-2S exhibits a noticeable photothermal performance, mainly attributed to the introduction of OVs significantly enhancing NIR light absorption intensity. When exposed to light, the crystal lattice vibrates, converting photon energy into thermal energy. To further evaluate the photothermal conversion performance of the B-2S samples, we tested the photothermal conversion efficiency, as shown in Fig. S9. The photothermal conversion efficiencies (η) of B-2S under 850 nm light irradiation were as high as 63.9%. The experimental results show that the combined action of oxygen vacancy and Bi_2S_3 contributes to the high photothermal conversion efficiency of B-2S, greatly improves the utilization rate of near infrared light and enhances

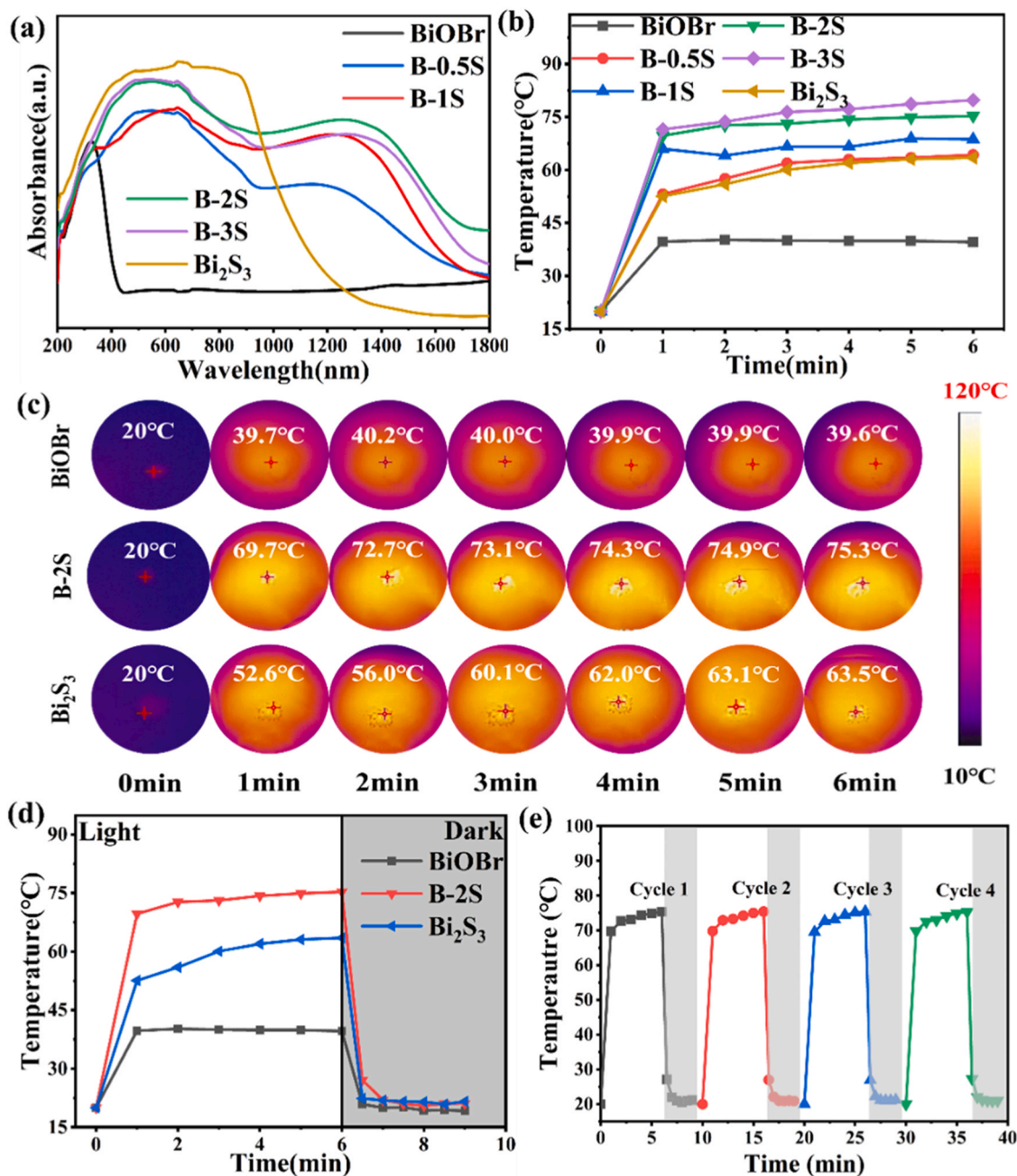


Fig. 3. (a) Absorption spectra; (b) Recorded temperature changes in samples under 850 nm light irradiation; (c) Thermal imaging of BiOBr, B-2S, and Bi₂S₃ under 850 nm light irradiation; (d) Recording temperature changes in samples during and after cessation of 850 nm light irradiation, and (e) Photothermal cycle curves (4 cycles) of B-2S.

the photothermal performance. Importantly, the photothermal effect raises the surface temperature of the photocatalyst under light, thereby sustaining the photocatalytic reaction at a higher temperature, which is advantageous for enhancing the photocatalytic activity.

To investigate the essential role of the BiOBr/Bi₂S₃ heterojunction constructed by the in-situ ion exchange method in light absorption and photothermal properties of the materials, BiOBr/Bi₂S₃ with different interface structures were synthesized by physical mixing and post-mixing hydrothermal methods at the same mass ratio, serving as reference samples. XRD experiments identified no significant differences in the crystal phase between the control sample and B-2S (Fig. S10a). Furthermore, it can be clearly seen from the absorption spectrum (Fig. S10b) that the absorption edge of the comparison sample is located around 1300 nm, similar to Bi₂S₃, and there is no characteristic

absorption peak of the LSPR effect of OVs. This further indicates that the generation of OVs comes from the process of in-situ growth of Bi₂S₃ through ion exchange on the BiOBr surface. Due to the lack of OVs, NIR absorption is weakened. Under NIR light irradiation at 850 nm, the temperatures of the physically mixed and mixed hydrothermal samples can only reach 60.4 °C and 57.7 °C, respectively (Fig. S10c), much lower than the temperature of B-2S under the same conditions, and even lower than the temperature of Bi₂S₃, confirming the important role of OVs in the photothermal effect. These results indicate that Bi₂S₃ and oxygen vacancies jointly promote the efficient photothermal performance of BiOBr/Bi₂S₃ heterojunctions.

3.3. Photocatalytic performance evaluation

To assess the photocatalytic efficiency of the fabricated samples, the typical heavy metal pollutant Cr(VI) was selected as the degradation target. As shown in Fig. 4a, it can be observed that the removal rates of BiOBr and Bi₂S₃ are 18% and 47% after 12 min of full-spectrum irradiation, respectively. This is due to their poor light utilization or rapid recombination of photogenerated carriers. Notably, after the incorporation of Bi₂S₃ into BiOBr, the degradation efficiency of Cr(VI) is significantly enhanced. This is caused by the capture of free electrons by OV's and the co-sharing atom interface, which accelerates charge transfer. Among them, B-2S showed the highest photocatalytic activity, achieving 100% Cr(VI) degradation within 10 min. According to the apparent rate constant (k) obtained by fitting the pseudo-first-order kinetic equation [50], the optimal B-2S heterojunction displayed the highest rate constant (0.4571 min^{-1}), which was approximately 31.97 and 8.67 times greater than those of BiOBr ($k = 0.0143 \text{ min}^{-1}$) and Bi₂S₃ ($k = 0.0527 \text{ min}^{-1}$), respectively (Fig. 4b). Additionally, B-2S ($k = 0.0699 \text{ min}^{-1}$) also exhibited efficient Cr(VI) reduction activity under NIR light irradiation, which was approximately 10.75 times greater than that of Bi₂S₃ ($k = 0.0065 \text{ min}^{-1}$), as shown in Fig. 4e and S12c. However, the photocatalytic activity decreased with the aggregation of excess Bi₂S₃ with further increases in Bi₂S₃ content. Excessive Bi₂S₃ can act as a charge recombination center and also influence the light absorption of BiOBr, resulting in a shading effect. It is evident that a BiOBr/Bi₂S₃ heterojunction with an appropriate content of Bi₂S₃ is

beneficial for improving photocatalytic performance and achieving the best synergistic effect. The reduction pathway of Cr(VI) was explored via XPS. Fig. 4c shows the high-resolution XPS of Cr 2p. The peaks located near 576.4 and 586.1 eV belong to Cr 2p_{3/2} and Cr 2p_{1/2}, confirming that the valence state of Cr was +3 [51]. The results indicate that the reduction reaction of Cr(VI) occurs, leading to a decrease in the valence state. This result confirms that Cr(VI) is indeed reduced to Cr(III) in the photocatalysis process. Compared to certain previously reported photocatalysts, the B-2S heterojunction also showed significant advantages in the photocatalytic reduction of Cr(VI) in the Vis-NIR range, as evidenced by Table S1, Fig. S12a, and Fig. S12b. The superior photocatalytic Cr(VI) reduction ability of the B-2S heterojunction can be attributed to the enhanced photoabsorption capacity (Fig. 3a) and effective separation and transfer of photogenerated carriers facilitated by the co-sharing atom interface and S-scheme heterojunction.

To investigate the essential role of the co-sharing atom interface constructed by the in-situ ion exchange method in photocatalytic performance, the photocatalytic performance of BiOBr/Bi₂S₃ synthesized by physical mixing and post-mixing hydrothermal method was tested. The Cr(VI) reduction rates of the mixing and post-mixing hydrothermal samples were only 46.2% and 23.6%, respectively, after 12 min of full-spectrum irradiation (Fig. S12d). This is much lower than that of the B-2S heterojunction. These results demonstrate that the intimate co-sharing of Bi atom interfaces between BiOBr and Bi₂S₃ plays an important role in enhancing photocatalytic performance. This effect, often described as “1 + 1 > 2,” should be attributed to the co-sharing Bi atom

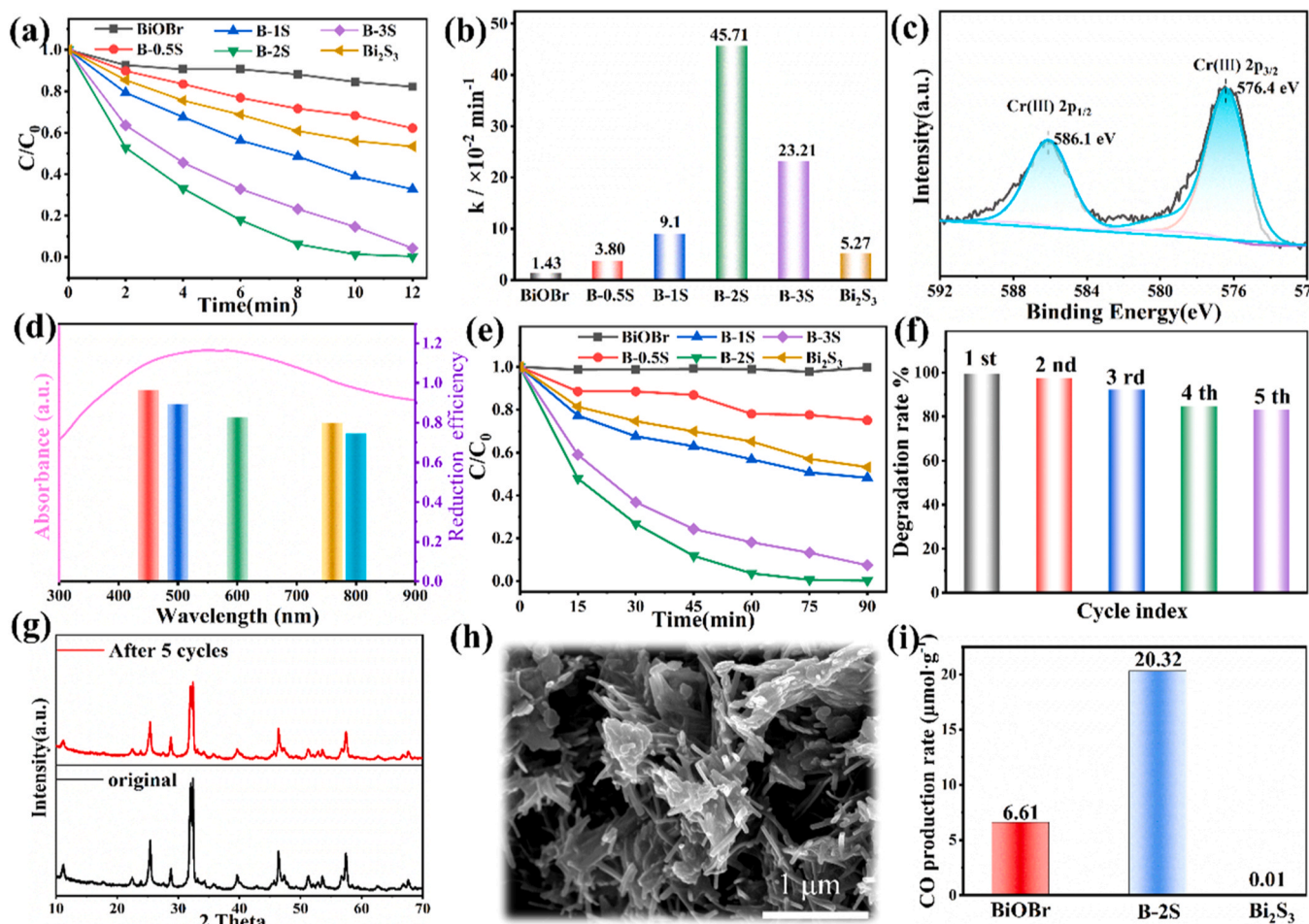


Fig. 4. (a) Cr(VI) reduction curves and (d) first-order-rate constants of different catalysts under full spectrum irradiation; (c) Cr fine spectrum of XPS after B-2S reaction; (d) Reduction efficiency of Cr(VI) by B-2S in 1 h under different wavelength light irradiation; (e) Cr(VI) reduction curves under NIR light irradiation; (f) Cycling experiment; (g) XRD and (h) SEM image patterns before and after five cycles of reaction; (i) Photocatalytic CO₂ reduction test.

interface facilitating charge transfer. These results further confirm that high-quality interfaces with strong chemical interactions and atomic-level close contact are formed in the BiOBr/Bi₂S₃ heterojunction through the in-situ growth of Bi₂S₃, which benefits from the strong built IEF at the interfaces, driving fast S-scheme spatial separation and transportation of photogenerated carriers. The distinctive benefits of this BiOBr/Bi₂S₃ heterojunction also suggest that a meticulously engineered structure greatly facilitates the uninterrupted transfer and segregation of charges. In addition, to evaluate the influence of photo-absorption on the photocatalytic activity of the B-2S heterojunction, experiments were conducted under monochromatic light with different emission wavelengths. Fig. 4d shows that the photocatalytic efficiency of monochromatic wavelengths has a significant wavelength dependence, which correlates well with the light absorption characteristics, indicating that light absorption plays a major role in photocatalytic performance.

Given the superb photocatalytic performance observed for the B-2S sample toward Cr(VI) reduction, recycling stability tests were carried out for practical applications. The Cr(VI) degradation efficiency of B-2S was still nearly 83.1% after 5 cycles of photocatalytic tests (Fig. 4f),

indicating excellent photocatalytic stability. Moreover, there were no significant changes in XRD, SEM, TEM, and XPS of B-2S after the recycling experiments (Fig. 4g, h, and S13), indicating the excellent stability of B-2S. This stability may be attributed to the strong combination between BiOBr and Bi₂S₃ through co-sharing Bi atoms. Therefore, the developed BiOBr/Bi₂S₃ heterojunction catalyst not only exhibits excellent performance stability but also demonstrates superb structural stability, making it promising for various applications. Fig. 4i shows the performance of different photocatalysts for photocatalytic CO₂ reduction. It can be observed that the CO evolution rate of the B-2S sample reached 20.32 $\mu\text{mol}\cdot\text{g}^{-1}$ under full-spectrum irradiation within 5 h, which is 3.07 times higher than that of BiOBr (6.61 $\mu\text{mol}\cdot\text{g}^{-1}$). The excellent CO₂ reduction performance of the BiOBr/Bi₂S₃ heterojunction catalyst lays the foundation for its potential use as a multifunctional catalyst.

3.4. Charge transfer path of S-scheme heterojunction

In accordance with the Kubelka-Munk equation [52], the energy bandgaps (E_g) of BiOBr and Bi₂S₃ were determined to be 2.86 and

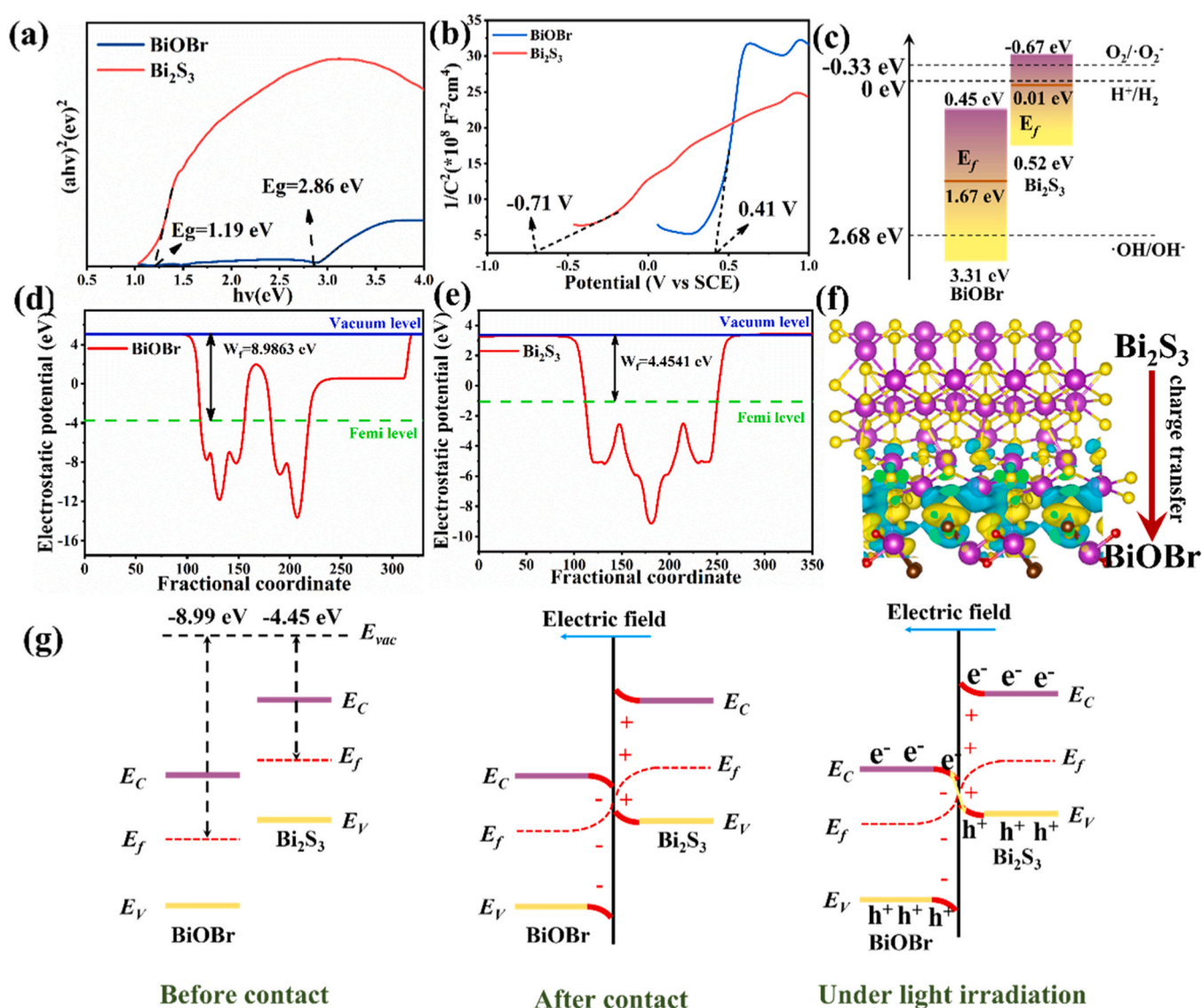


Fig. 5. (a) Bandgap energies and (b) Mott-Schottky plots of BiOBr and Bi₂S₃; (c) Schematic energy band structure of BiOBr and Bi₂S₃; Electrostatic potentials of (d) BiOBr and (e) Bi₂S₃ determined by DFT; (f) Charge density distribution of BiOBr/Bi₂S₃ heterojunctions, the blue and yellow colors represent the electron depletion and accumulation region; (g) Relative energy band positions and the S-scheme charge transfer mechanism between pristine BiOBr and Bi₂S₃.

1.19 eV, respectively, as illustrated in Fig. 5a. Additionally, semiconductor types and corresponding flat-band potentials (E_{FB}) were identified through Mott-Schottky (M-S) measurements. As depicted in Fig. 5b, both BiOBr and Bi_2S_3 exhibited positive slopes in their M-S plots, indicating n-type semiconductor characteristics. The E_{FB} of BiOBr and Bi_2S_3 were verified to be 0.41 V and -0.71 V vs. SCE (0.65 V and -0.47 V vs. NHE) [53]. Generally, the conduction band potential (E_{CB}) of an n-type semiconductor is 0.2 eV more negative compared to E_{FB} [54]. Hence, the E_{CB} values for BiOBr and Bi_2S_3 were established as 0.45 and -0.67 eV (vs. NHE), respectively. Moreover, following the empirical

formula: $E_{VB} = E_{CB} + E_g$ [55], the E_{VB} values for BiOBr and Bi_2S_3 were calculated to be 3.31 eV and 0.52 eV, respectively. Consequently, Bi_2S_3 takes on the role of RP, while BiOBr functions as OP. Additionally, the energy gap energies between the Fermi level (E_f) and VB of BiOBr and Bi_2S_3 , obtained from the VB-XPS spectra, were 1.01 and 1.60 eV, respectively (Fig. S14). Hence, E_f values for BiOBr and Bi_2S_3 were determined as 1.67 V and 0.01 V, respectively [56]. Based on the above analysis, the schematic energy band structure of BiOBr and Bi_2S_3 is depicted in Fig. 5c. The staggered energy band structure between them is a crucial factor contributing to the formation of the S-scheme

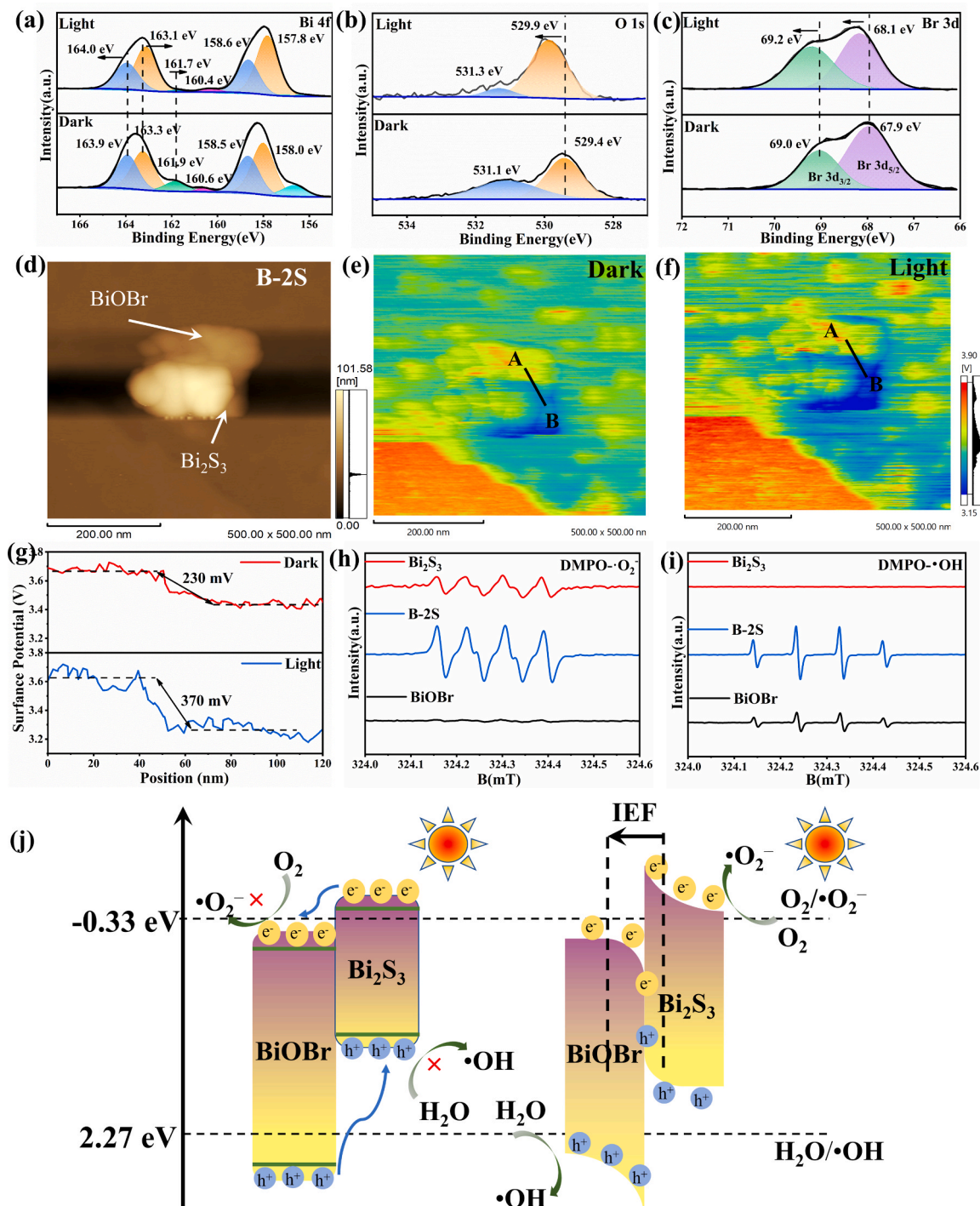


Fig. 6. In situ irradiated XPS of (a) Bi 4f, (b) O 1s and (c) Br 3d of B-2S; KPFM study of the B-2S heterojunction: (d) AFM height image, (e-g) Surface potential distribution in darkness and light illumination; EPR spectra of the (h) DMPO- $\cdot O_2^-$ and (i) DMPO- $\cdot OH$ for B-2S under full-spectrum light irradiation; (j) Photogenerated e^- and h^+ pair separation and possible reaction mechanistic pathway of BiOBr/ Bi_2S_3 heterojunctions.

heterojunction.

To further elucidate the S-scheme mechanism of the BiOBr/Bi₂S₃ heterojunction, we employed density functional theory (DFT) for investigation. As depicted in Fig. 5d and e, DFT calculations revealed the work function (Φ) of BiOBr to be 8.98 eV and that of Bi₂S₃ to be 4.45 eV. This indicates that the E_f of BiOBr is significantly lower than that of Bi₂S₃. Upon contact between BiOBr and Bi₂S₃, electrons from Bi₂S₃ spontaneously transfer to BiOBr across their interface to achieve E_f equilibrium. Consequently, at equilibrium, the interface of Bi₂S₃ carries a positive charge due to the loss of electrons, causing an upward bending of the interfacial band. In contrast, BiOBr acquires a negative charge at the interface due to the increased electron cloud density, resulting in a downward bending of the interfacial band. This leads to the generation of an IEF from Bi₂S₃ to BiOBr. Furthermore, the differential charge density plot of the BiOBr/Bi₂S₃ heterostructure (Fig. 5f) clearly illustrates the charge transfer between BiOBr and Bi₂S₃, with blue and yellow regions representing electron depletion and accumulation, respectively. Notably, charge redistribution near the interface occurs when BiOBr and Bi₂S₃ come into contact. Interestingly, we observe an O-Bi-S bond channel for charge transfer at the interface (Fig. 5f), where electrons in Bi₂S₃ preferentially transfer into BiOBr through this channel. When subjected to light illumination, both BiOBr and Bi₂S₃ generate electron-hole pairs (e^- and h^+). Under the combined influence of interfacial band bending and the IEF, photogenerated electrons in the CB of BiOBr rapidly transfer across the interface and recombine with photogenerated holes in the VB of Bi₂S₃, preserving the photogenerated holes on the VB of BiOBr and the photogenerated electrons on the CB of Bi₂S₃ (Fig. 5g). Consequently, an S-scheme heterojunction is formed between BiOBr and Bi₂S₃.

To gain further insights into the charge transfer mechanism of BiOBr/Bi₂S₃ heterojunctions, in-situ XPS and photoassisted Kelvin probe force microscopy (KPFM) were employed under irradiation [57]. The binding energies of Bi₂S₃-Bi 4 f and S 2p under light irradiation shifted to lower values compared to those in the dark, whereas BiOBr-Bi 4 f shifted to higher energies (Fig. 6a). Similar trends were observed in the O 1 s and Br 3d spectra (Fig. 6b and c). These shifts in binding energies indicate an increase in electron density in Bi₂S₃ and a decrease in electron density in BiOBr under light illumination, confirming the migration of photogenerated electrons in the CB of BiOBr to the VB of Bi₂S₃, supporting the proposed S-scheme charge-transfer mechanism. Subsequently, the interfacial charge transfer behavior of the BiOBr/Bi₂S₃ photocatalyst was studied using KPFM. As shown in Fig. 6d-g, the surface potential of Bi₂S₃ is approximately 230 mV lower than that of BiOBr in the dark. Interestingly, under light irradiation, the surface potential of the Bi₂S₃ part decreases significantly, and the potential difference between BiOBr and Bi₂S₃ increases to 370 mV. This phenomenon suggests the accumulation of photogenerated electrons on the surface of Bi₂S₃, providing further evidence for the S-scheme charge-transfer mechanism in the BiOBr/Bi₂S₃ heterojunction.

The ESR was employed as an effective technique to detect spin-active hydroxyl radicals (\bullet OH) and superoxide radicals (\bullet O₂⁻), providing strong evidence for exploring the direction of electron transfer. Thus, ESR measurements were conducted using 5,5-dimethyl-1-pyrroline N-oxide (DMPO) as the trapping agent to further validate the BiOBr/Bi₂S₃ S-scheme heterostructure. As presented in Fig. 6h, the DMPO- \bullet O₂⁻ signal of Bi₂S₃ and B-2S heterojunction is clearly observed, while the DMPO- \bullet O₂⁻ signal of pristine BiOBr was hardly detected. Moreover, clear DMPO- \bullet OH signals were observed in BiOBr and B-2S heterojunction, whereas Bi₂S₃ showed no signal (Fig. 6i). This is attributed to the reduction potential of the CB of Bi₂S₃ (-0.67 eV) being more negative than the potential for O₂/ \bullet O₂⁻ (-0.33 eV vs. NHE), while the oxidation potential of the VB of BiOBr (3.31 eV) is more positive than the redox potential of H₂O/ \bullet OH (2.27 eV vs. NHE) [27]. Notably, both DMPO- \bullet O₂⁻ and DMPO- \bullet OH signals of the B-2S heterojunction are significantly stronger compared to those of pure BiOBr and Bi₂S₃, indicating that more photogenerated holes can accumulate on the VB of BiOBr in the B-2S

heterojunction. The EPR results strongly support the conclusion that photogenerated carriers in the BiOBr/Bi₂S₃ heterojunction follow the S-scheme transfer route. The previously discussed band structure, DFT calculations, in-situ XPS spectra, KPFM, and EPR characterization provide substantial evidence for the S-scheme charge-transfer path between BiOBr and Bi₂S₃ in the heterojunction photocatalyst (Fig. 6j). This S-scheme heterojunction charge-transfer mechanism not only greatly enhances the separation efficiency of photogenerated charges but also maximizes the retention of e^- and h^+ with strong reducing and oxidizing capacities, respectively, resulting in a significant improvement in photocatalytic performance.

3.5. Charge carrier dynamics behavior

Based on the aforementioned results, a high-quality BiOBr/Bi₂S₃ S-scheme heterojunction was successfully prepared. To investigate how this heterojunction affects the charge separation of the photocatalysts, we conducted a series of photoelectrochemical measurements to elucidate the charge transfer kinetics of the samples. Fig. 7a shows the photocurrent response of BiOBr, Bi₂S₃, and BiOBr/Bi₂S₃ heterojunctions under full-spectrum irradiation. It is evident that the BiOBr/Bi₂S₃ heterojunctions exhibited significantly higher photocurrent density compared to BiOBr and Bi₂S₃, demonstrating the superior charge carrier separation efficiency of the BiOBr/Bi₂S₃ heterojunction. Furthermore, the separation of photogenerated e^- and h^+ at the photocatalyst/electrolyte interface results in spikes in the current curve [58]. We further supported these results with electrochemical impedance spectroscopy (EIS) data, as depicted in Fig. 7b. The B-2S heterojunction exhibited the smallest semicircle, indicating the lowest charge transfer resistance (R_{ct}) [59]. The R_{ct} values were obtained by fitting the EIS curve, as shown in Table S2. It can be observed that the R_{ct} of B-2S (30.3 k Ω) decreased significantly compared to that of pristine BiOBr (150.0 k Ω) and Bi₂S₃ (110.1 k Ω), further confirming that the formation of an atom co-sharing Bi atom interfacial between BiOBr and Bi₂S₃ reduces the interfacial charge transfer resistance. This reduction is favorable for the separation and migration of photogenerated carriers. Therefore, the higher photocurrent response and smaller resistance of B-2S indicate excellent charge separation efficiency, which can be attributed to the formation of atom co-sharing S-scheme heterojunctions.

To better assess the recombination of photogenerated carriers, we conducted photoluminescence (PL) and time-resolved photoluminescence (TRPL) spectroscopy tests on the samples. As shown in Fig. 7c, pure BiOBr exhibited the highest PL intensity, indicating the highest recombination rate of photogenerated e^- and h^+ pairs, which led to lower photocatalytic activity, consistent with the catalytic experiment results (Fig. 4). After combining BiOBr and Bi₂S₃, the PL intensity of Bi₂S₃/BiOBr heterojunctions noticeably decreased, and B-2S had the lowest PL intensity. This suggests that the construction of the Bi₂S₃/BiOBr heterojunction significantly inhibits the recombination of photogenerated carriers, aligning with the photocurrent responses and EIS measurements. This inhibition occurs because a heterojunction is formed between BiOBr and Bi₂S₃, and the Bi₂S₃/BiOBr interfaces facilitate charge transfer through atomic-level interfacial contacts, resulting from the co-sharing of the Bi atom. The introduction of OV's effectively restricts the recombination of photogenerated e^- - h^+ pairs, further enhancing photocatalytic efficiency. Additionally, we investigated the photogenerated carrier transfer using TRPL spectra (Fig. 7d). The decay curves were fitted by a double-exponential function [60]. As shown in Table 1, the average fluorescence lifetime (τ_A) of B-2S (1.50 ns) was longer than that of pure BiOBr (0.86 ns) and Bi₂S₃ (1.19 ns), indicating that the formation of the heterojunction promotes the separation and migration of photogenerated carriers. The extension of carrier lifetime in the BiOBr/Bi₂S₃ heterojunctions may be attributed to the atom co-sharing S-scheme heterojunction, which accelerates carrier separation and migration, maximizing the utilization efficiency of photogenerated carriers in the photocatalytic process. This finding aligns with

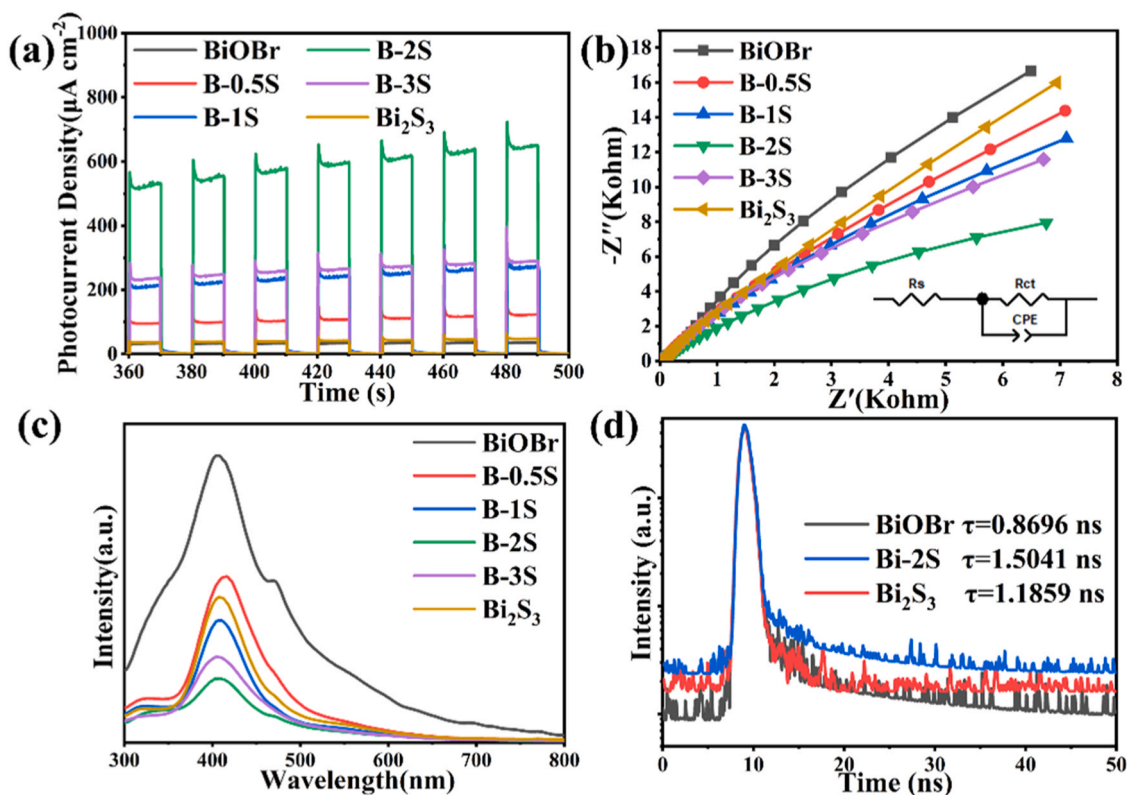


Fig. 7. (a) Transient photocurrent response; (b) EIS; (c) PL spectra; (d) TRPL spectra of BiOBr/ Bi_2S_3 heterojunctions.

Table 1

Kinetic parameters for fitting decay parameters of BiOBr, Bi_2S_3 , and B-2S heterojunction.

Samples	τ_1 [ns]	A_1 [%]	τ_2 [ns]	A_2 [%]	τ_A [ns]
BiOBr	0.50	92.59	5.46	7.41	0.8696
B-2S	0.57	91.01	11.00	8.99	1.5041
Bi_2S_3	0.59	90.61	6.91	9.39	1.1859

the results from transient photocurrent responses, EIS analysis, and PL spectra. These results collectively suggest that highly efficient charge separation between BiOBr and Bi_2S_3 can be achieved by constructing atom co-sharing S-scheme heterojunctions with IEF. The co-sharing of the Bi atom serves as an atomic-level charge transfer channel, facilitating rapid charge migration and increasing its contribution to photocatalytic reactions.

3.6. Contribution of photothermal effect

In the photocatalysis process, the photothermal effect plays a vital role in improving photocatalytic activity. This is because an increase in temperature accelerates the migration of photoexcited charges and enhances surface reaction kinetics, significantly boosting photocatalytic activity. To explore the contribution of the photothermal effect to enhancing photocatalytic activity, we investigated the photocatalytic reduction of Cr(VI) at different temperature systems. As shown in Fig. 8a, only 50% of Cr(VI) can be reduced within 12 min at 20 °C ($k = 0.0727 \text{ min}^{-1}$). However, when the temperature is increased to 60 °C, Cr(VI) can be completely reduced within 10 min ($k = 0.5004 \text{ min}^{-1}$), resulting in a 6.9-fold increase in catalytic efficiency (Fig. 8b). This efficiency is even higher than the full spectrum catalytic efficiency ($k = 0.4571 \text{ min}^{-1}$) at room temperature. To exclude the influence of heat on Cr(VI) reduction, we examined the activity of B-2S for the thermal decomposition of Cr(VI) at 60 °C in a comparative

experiment. The results showed that the Cr(VI) reduction rate was 0% (Fig. S15), suggesting that pure thermal catalysis had no contribution to the reduction of Cr(VI). These results indicate that the thermal effect induced by the photothermal effect of the catalyst plays an auxiliary role in the photocatalytic process. In the process of photothermal catalytic reduction of Cr(VI), the thermal energy produced from the photothermal effect could expedite charge transfer and promote effective separation of e^-h^+ pairs, thereby enhancing photocatalytic performance.

Furthermore, it should be noted that practical photocatalytic reactions take place in aqueous solutions. Therefore, it is necessary to further consider and study the influence of the photothermal effect of the catalyst on the temperature of the reaction solution. We measured the temperature change of the solution without temperature control (20 mg of catalysts were added to 40 mL of Cr(VI) solution). After 15 min of continuous NIR light exposure, the temperature stabilized (Fig. 8c). The temperature of the Cr(VI) solution with BiOBr and Bi_2S_3 was 46.2 °C and 59.4 °C, respectively, while the Cr(VI) solution with B-2S reached a temperature of 74 °C. This indicates that the photothermal effect of B-2S under NIR light irradiation can effectively increase the temperature of the catalytic environment, providing conditions for photothermal collaborative catalysis. It is evident that the efficient photothermal effect of B-2S can effectively enhance the catalytic ambient temperature, providing ideal conditions for photothermal collaborative catalysis and greatly promoting catalytic efficiency.

To further assess the influence of photothermal effects on the dynamics of photogenerated carriers in the catalyst, we conducted photoelectrochemical characterizations at different temperatures. As shown in Fig. 8d and f, higher temperatures resulted in higher photocurrent intensity and lower impedance. This effect is due to the fact that higher temperatures effectively enhance the excitation of photogenerated e^-h^+ pairs, reduce carrier transport resistance, promote the separation and transfer of carriers, and significantly reduce carrier recombination [61]. According to the principles of semiconductor physics, there is a relationship between temperature (T), charge carrier transport rate (μ), and

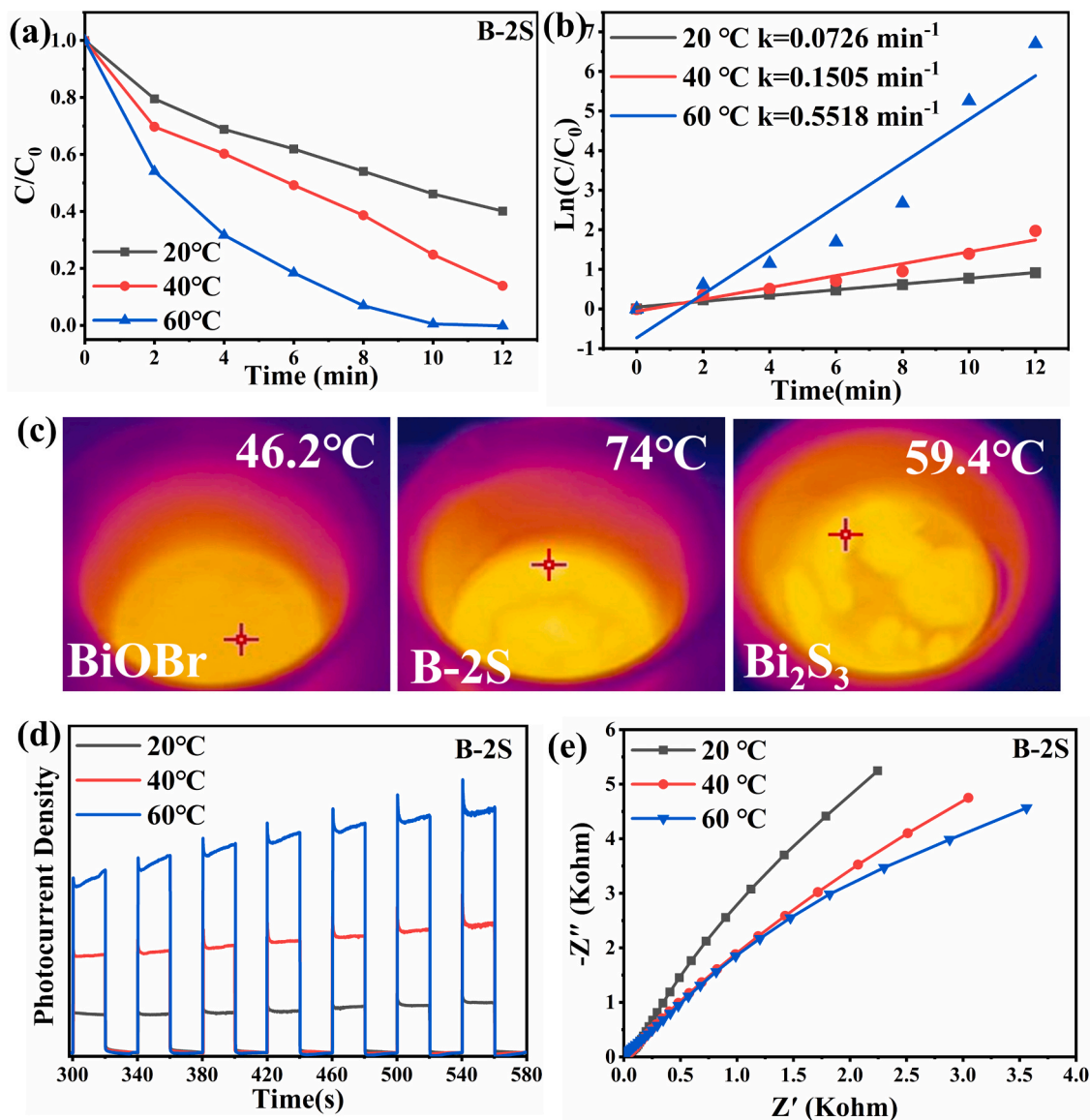


Fig. 8. (a) Efficiency of Cr(VI) NIR photocatalytic reduction by B-2S at various temperatures; (b) First-order rate constants; (c) Photothermal IR images during NIR light irradiation; (d) Photocurrent response and (e) EIS curves of B-2S samples at different temperatures.

the resistivity (ρ) of semiconductors, as follows [62]:

$$\mu \propto \left[\exp\left(\frac{h\omega}{2\pi k_0 T}\right) - 1 \right] \quad (1)$$

$$\rho = \frac{1}{nq\mu_n + pq\mu_p} \quad (2)$$

In formula (1), h , ω , and k_0 represent Planck's constant, angular frequency, and Boltzmann's constant, respectively. According to this formula, it can be inferred that as the temperature (T) increases, μ also increases. In formula (2) n , p , q , and μ are the concentrations of electrons, concentrations of holes, charge quantity, and charge transfer rate of n-type and p-type semiconductors, respectively. It is clear that larger μ_n and μ_p result in smaller ρ . In summary, temperature is a key factor affecting the dynamics of photogenerated carriers, especially in photocatalytic reactions under high-temperature conditions. This effect can effectively improve the separation and transfer of photogenerated carriers.

3.7. Photocatalytic mechanism

The photogenerated electrons play a crucial role in the process of photocatalytic reduction. To investigate the possible mechanism of photocatalytic removal of Cr(VI) by the prepared B-2S heterojunction, we examined the effect of potential active substances on Cr(VI). Silver nitrate (AgNO_3) was used to capture e^- , Ethylenediaminetetraacetic acid disodium salt (EDTA) served as scavengers for h^+ , Isopropyl alcohol (IPA) acted as scavengers for hydroxyl radicals ($\bullet\text{OH}$), and Benzoquinone (BQ) was utilized as scavengers for superoxide radicals ($\bullet\text{O}_2^-$) (Fig. S17). Compared to the reaction without scavengers, the Cr(VI) reduction rate sharply decreased after adding AgNO_3 because electrons were captured by AgNO_3 instead of being transferred to Cr(VI) ions for photoreduction. However, the reduction rate only slightly decreased after adding EDTA, possibly due to the formation of a hydrogen bond between the carboxylic group of the hole scavenger and the OH group of the photocatalyst. This bond impedes the electrostatic adsorption of Cr(VI) anions on positively charged groups of the photocatalyst during photocatalysis [63]. Moreover, the reduction rate of Cr(VI) after adding IPA or BQ had little effect. These results indicate that e^- are the active

species responsible for the photocatalytic Cr(VI) reduction.

Furthermore, the photocatalytic mechanism of Cr(VI) reduction in the BiOBr/Bi₂S₃ heterojunction was revealed through DFT calculations. Fig. 9a shows the electron density difference of Cr₂O₇²⁻ adsorbed on the surfaces of BiOBr, B-2S, and Bi₂S₃, indicating electron transfer from BiOBr, B-2S, and Bi₂S₃ to Cr₂O₇²⁻. Using the Bader charge analysis method, we estimated that 1.33, 1.36, and 1.96 electrons (Δq) were transferred from BiOBr, B-2S, and Bi₂S₃ to Cr₂O₇²⁻, respectively. Additionally, we calculated the adsorption energies (E_{ads}) of Cr₂O₇²⁻ adsorbed on the surfaces of BiOBr, B-2S, and Bi₂S₃ to be -1.85, -2.17, and -1.93 eV, respectively. These results suggest that B-2S is more effective at adsorbing and activating Cr₂O₇²⁻. The Gibbs free energy of elementary reaction steps for Cr₂O₇²⁻ reduction into Cr(OH)₃ on the surfaces of BiOBr, B-2S, and Bi₂S₃, along with the corresponding optimized structures of intermediates, are depicted in Fig. 9b and c. All reaction steps for both BiOBr, B-2S, and Bi₂S₃ were found to be thermodynamically favorable, as indicated by negative Gibbs free energy values. Initially, *Cr₂O₇ formed on the catalyst surfaces. Subsequently, *Cr₂O₇H was generated through hydrogenation of *Cr₂O₇, followed by dissociation into H₂O and *Cr₂O₆. Furthermore, *Cr₂O₆ split into two *CrO₃ molecules, capable of accepting two electron-proton pairs to form *CrO₃H and *CrO₃H₂, which were ultimately converted into *Cr(OH)₃ [64].

Notably, the Gibbs free energy of the B-2S/Cr₂O₇²⁻ system was noticeably higher than that of the other systems during the elementary reaction steps, indicating that B-2S is more conducive to reducing Cr₂O₇²⁻ into Cr(OH)₃.

Based on the results of experimental and theoretical calculations, we propose a potential photocatalytic enhancement mechanism for the BiOBr/Bi₂S₃ heterojunction, as illustrated in Fig. 10. Under light irradiation, e⁻-h⁺ pairs are generated simultaneously at both BiOBr and Bi₂S₃. The photogenerated e⁻ in the CB of BiOBr combine with the h⁺ in the VB of Bi₂S₃ due to the presence of an internal electric field at the contact interface between BiOBr and Bi₂S₃. Thus, h⁺ accumulate in the VB of BiOBr, while e⁻ accumulate in the CB of Bi₂S₃. Subsequently, e⁻ on Bi₂S₃ react with Cr(VI) and CO₂, reducing Cr(VI) to Cr(III) and CO₂ to CO. Additionally, the co-sharing of Bi atoms provides an atomic-level interfacial channel between BiOBr and Bi₂S₃, facilitating charge transfer and promoting the S-scheme charge transfer process. Furthermore, Bi₂S₃ and OVns induce an LSPR effect, which broadens the spectral response from UV-visible to NIR, enabling the photocatalyst to fully utilize solar energy. This effect also enhances the photothermal effect, which accelerates charge carrier transport and surface reaction kinetics. In summary, the synergistic effects of the S-scheme heterojunctions, atomic-level interfacial channels, OVns, and high photothermal efficiency

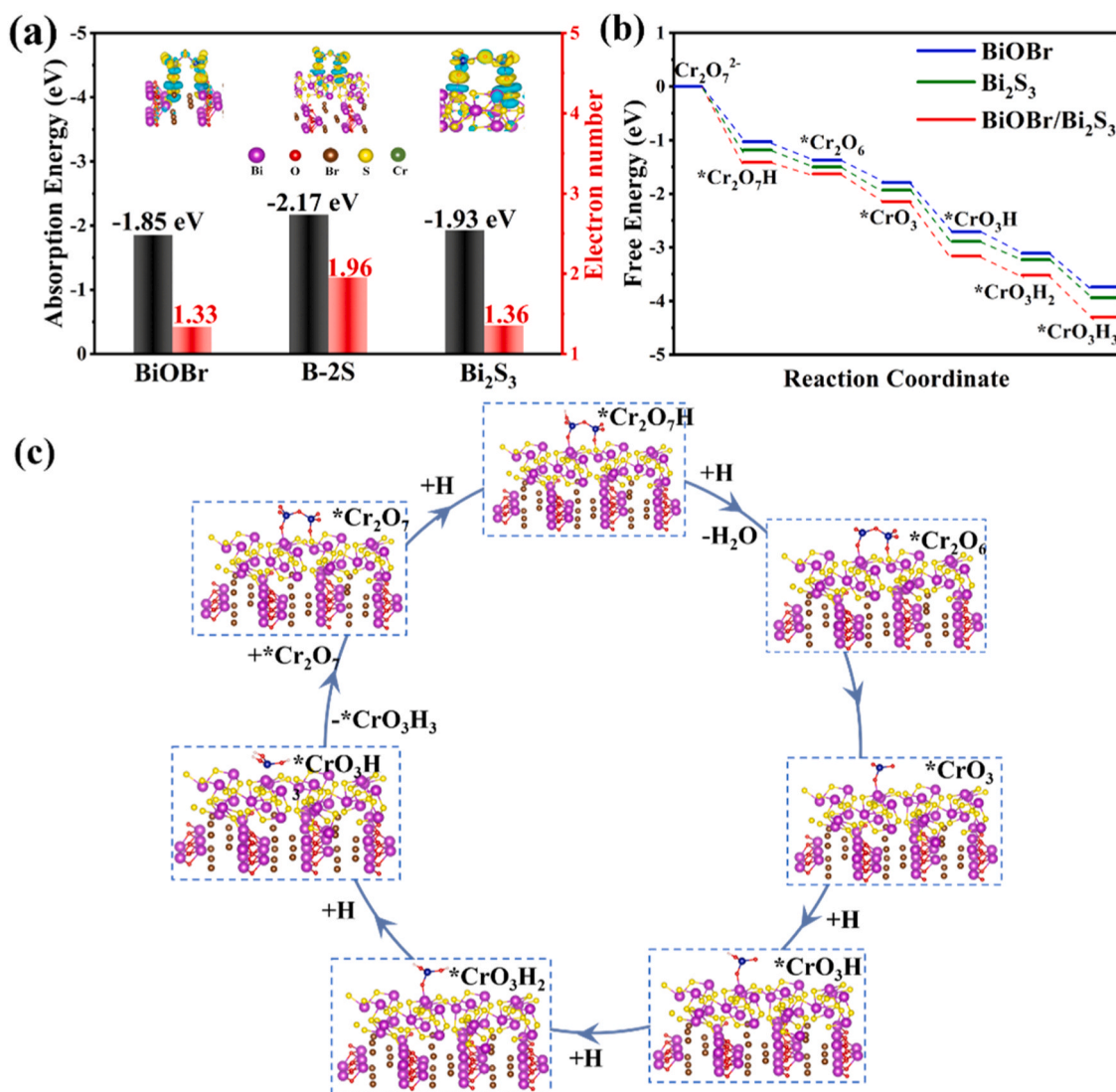


Fig. 9. (a) Electron density difference of Cr(VI) adsorbed on BiOBr, B-2S, and Bi₂S₃ surfaces; (b) Gibbs free energy of Cr(VI) reduction over BiOBr, B-2S, and Bi₂S₃; (c) Optimized structures of intermediates over B-2S during Cr(VI) reduction processes.

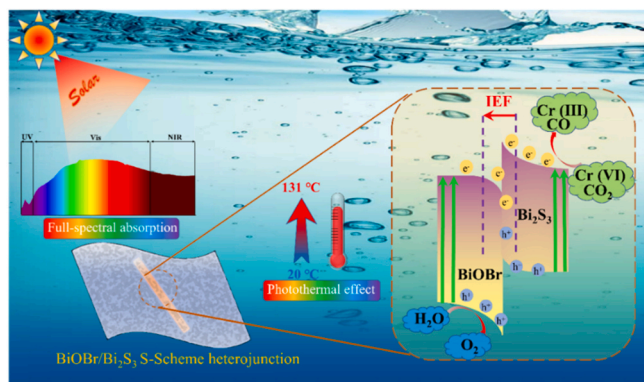


Fig. 10. Schematic diagram of the photocatalytic mechanism of BiOBr/Bi₂S₃ under light irradiation.

result in strong interface interactions between components, expanding the spectral absorption range, enhancing the separation and utilization efficiency of photoinduced carriers, and enhancing the photocatalytic reduction of Cr(VI) and CO₂ by the BiOBr/Bi₂S₃ heterojunction.

4. Conclusion

In summary, we successfully designed and constructed an S-scheme BiOBr/Bi₂S₃ heterojunction with co-sharing Bi atoms using an ion exchange approach and in-situ growth process. This heterojunction demonstrated excellent photocatalytic reduction performance for Cr(VI) and CO₂. Under full solar-spectrum irradiation, B-2S achieved a Cr(VI) photoreduction rate of 100% within 10 min and produced 20.32 μmol·g⁻¹ of CO after 5 h of irradiation. These values were 31.97 and 3.07 times higher than those of BiOBr, respectively. This superior photocatalytic performance can be attributed to several synergistic effects: (1) Bi₂S₃ and OVs induced LSPR effect broadens the light response range and enhances light harvesting ability; (2) S-scheme heterojunctions promote the separation and migration of carriers and retain a large number of photogenerated carriers with high redox potentials, supported by DFT, in situ irradiated XPS, KPFM, and EPR analysis; (3) Co-sharing of Bi atoms furnishes an atomic-level interfacial channel, reduces interface resistance, and facilitates charge transfer; (4) the photothermal effect further improves charge transfer and accelerates surface reaction kinetics. This work provides significant guidance and systematic research methods for the development of efficient, stable, and low-cost S-scheme photothermal catalysts with full spectral response.

CRediT authorship contribution statement

Junhao Ma: Writing - original draft, Conceptualization, Methodology, Software, Investigation. **Liang Xu:** Methodology, Formal analysis, Visualization. **Zhaoyi Yin:** Conceptualization, Writing - review & editing. **Zhifeng Li:** Conceptualization, Writing - review & editing. **Xiaoyi Dong:** Writing - review & editing. **Zhiguo Song:** Funding acquisition, Supervision. **Daomei Chen:** Conceptualization. **Rui Hu:** Funding acquisition. **Qi Wang:** Supervision, Validation. **Jin Han:** Supervision, Validation. **Zhengwen Yang:** Funding acquisition. **Jianbei Qiu:** Supervision, Validation. **Yongjin Li:** Funding acquisition, Supervision, Validation, Writing - review & editing.

Declaration of Competing Interest

The authors declare that they have no known competing financial interests or personal relationships that could have appeared to influence the work reported in this paper.

Data Availability

Data will be made available on request.

Acknowledgements

This work was supported by the National Natural Science Foundation of China (No. 12204207), the National Natural Science Foundation of China-Yunnan Joint Fund (No. U2102215), the National Natural Science Foundation of High and Foreign Experts Introduction Plan (No. G2022039008L), and Yunnan XingDian Youth Talent Support Program (No. XDYC-QNRC-2022-0591). We thank Shiyanjia Lab (<https://www.shiyanjia.com>) for the XRD and XPS analysis, and we also thank SCI-GO (<https://www.sci-go.com>) for the DFT calculations.

Appendix A. Supporting information

Supplementary data associated with this article can be found in the online version at [doi:10.1016/j.apcatb.2023.123601](https://doi.org/10.1016/j.apcatb.2023.123601).

References

- [1] D. Kim, K.K. Sakimoto, D.C. Hong, P.D. Yang, Artificial photosynthesis for sustainable fuel and chemical production, *Angew. Chem. Int. Ed.* 54 (2015) 3259–3266.
- [2] Y.J. Yuan, Z.T. Yu, D.Q. Chen, Z.G. Zou, Metal-complex chromophores for solar hydrogen generation, *Chem. Soc. Rev.* 46 (2017) 603–631.
- [3] W.-J. Ong, Learning from natural leaves: going green with artificial photosynthesis forum, *ACS Appl. Mater. Inter.* 11 (2019) 5579–5580.
- [4] H. Li, F. Deng, Y. Zheng, L. Hua, C. Qu, X. Luo, Visible-light-driven Z-scheme rGO/Bi₂S₃-BiOBr heterojunctions with tunable exposed BiOBr (102) facets for efficient synchronous photocatalytic degradation of 2-nitrophenol and Cr(VI) reduction, *Environ. Sci. Nano* 6 (2019) 3670–3683.
- [5] Y. Xi, W. Mo, Z. Fan, L. Hu, W. Chen, Y. Zhang, P. Wang, S. Zhong, Y. Zhao, S. Bai, A mesh-like BiOBr/Bi₂S₃ nanoarray heterojunction with hierarchical pores and oxygen vacancies for broadband CO₂ photoreduction, *J. Mater. Chem. A* 10 (2022) 20934–20945.
- [6] T. Wang, Y. Wang, W. Fan, R. Wu, Q. Liang, J. Hao, Boosting room-temperature NO₂ detection via in-situ interfacial engineering on Ag₂S/SnS₂, *Heterostruct., J. Hazard. Mater.* 434 (2022), 128782.
- [7] Y. Yu, T. Ma, H. Huang, Semiconducting quantum dots for energy conversion and storage, *Adv. Funct. Mater.* 33 (2023) 2213770.
- [8] J. Zhang, Y. Zhao, K. Qi, S.-y. Liu, CuInS₂ quantum-dot-modified g-C₃N₄ S-scheme heterojunction photocatalyst for hydrogen production and tetracycline degradation, *J. Mater. Sci. Technol.* 172 (2024) 145–155.
- [9] A. Meng, L. Zhang, B. Cheng, J. Yu, Dual cocatalysts in TiO₂ photocatalysis, *Adv. Mater.* 31 (2019) 1807660.
- [10] J. Zhang, A. Bifulco, P. Amato, C. Imparato, K. Qi, Copper indium sulfide quantum dots in photocatalysis, *J. Colloid Interface Sci.* 638 (2023) 193–219.
- [11] Y. Yang, H. Tan, B. Cheng, J. Fan, J. Yu, W. Ho, Near-infrared-responsive photocatalysts, *Small Methods* 5 (2021) 2001042.
- [12] J. Lu, Y. Shi, Z. Chen, X. Sun, H. Yuan, F. Guo, W. Shi, Photothermal effect of carbon dots for boosted photothermal-assisted photocatalytic water/seawater splitting into hydrogen, *Chem. Eng. J.* 453 (2023), 139834.
- [13] Q. Xu, L. Zhang, B. Cheng, J. Fan, J. Yu, S-scheme heterojunction photocatalyst, *Chem* 6 (2020) 1543–1559.
- [14] W. Yu, J. Chen, T. Shang, L. Chen, L. Gu, T. Peng, Direct Z-scheme g-C₃N₄/WO₃ photocatalyst with atomically defined junction for H₂ production, *Appl. Catal. B.* 219 (2017) 693–704.
- [15] Y. Xia, B. Zhu, X. Qin, W. Ho, J. Yu, Zinc porphyrin/g-C₃N₄ S-scheme photocatalyst for efficient H₂O₂ production, *Chem. Eng. J.* 467 (2023), 143528.
- [16] M. Mousavi, A. Bonakdar, A. Parsaei-Khomami, J.B. Ghasemi, P. Pourhakkak, M. M. Habibi, M. Jafari, A.H. Jalili, X. Li, Visible-light-driven g-C₃N₄/AgBiS₂ S-scheme photocatalyst for N₂ fixation and rhodamine B degradation, *J. Phys. Chem. Solids* 179 (2023), 111376.
- [17] J. Huang, B. Zhu, D. Song, B. Wang, L. Chen, L. Lu, Q. Chen, L. Gai, C. Zhai, L. Chen, H. Tao, Synergistic photocatalysis for naphthalene (NAP) removal in seawater by S-scheme heterojunction Bi₂S₃/CeVO₄: mechanistic investigation and degradation pathways, *Chem. Eng. J.* 464 (2023), 142784.
- [18] C. Wang, H. Liu, G. Wang, H. Fang, X. Yuan, C. Lu, Photocatalytic removal of metronidazole and Cr(VI) by a novel Zn₃In₂S₆/Bi₂O₃ S-scheme heterojunction: performance, mechanism insight and toxicity assessment, *Chem. Eng. J.* 450 (2022), 138167.
- [19] Q. Cui, X. Gu, Y. Zhao, K. Qi, Y. Yan, S-scheme CuInS₂/ZnS heterojunctions for the visible light-driven photocatalytic degradation of tetracycline antibiotic drugs, *J. Taiwan. Inst. Chem. Eng.* 142 (2023), 104679.
- [20] H. Wang, C. Qian, J. Liu, Y. Zeng, D. Wang, W. Zhou, L. Gu, H. Wu, G. Liu, Y. Zhao, Integrating suitable linkage of covalent organic frameworks into covalently

- bridged inorganic/organic hybrids toward efficient photocatalysis, *J. Am. Chem. Soc.* 142 (2020) 4862–4871.
- [21] Z.-L. Liu, R.-R. Liu, Y.-F. Mu, Y.-X. Feng, G.-X. Dong, M. Zhang, T.-B. Lu, In situ construction of lead-free perovskite direct Z-scheme heterojunction $\text{Cs}_3\text{Bi}_2\text{I}_9/\text{Bi}_2\text{WO}_6$ for efficient photocatalysis of CO_2 reduction, *Sol. RRL* 5 (2021) 2000691.
- [22] X.-D. Wang, Y.-H. Huang, J.-F. Liao, Y. Jiang, L. Zhou, X.-Y. Zhang, H.-Y. Chen, D.-B. Kuang, In situ construction of a Cs_2SnI_6 perovskite nanocrystal/ SnS_2 nanosheet heterojunction with boosted interfacial charge transfer, *J. Am. Chem. Soc.* 141 (2019) 13434–13441.
- [23] D. Kaur, V. Bagga, N. Behera, B. Thakral, A. Asija, J. Kaur, S. Kaur, SnSe/SnO_2 nanocomposites: novel material for photocatalytic degradation of industrial waste dyes, *Adv. Compos. Hybrid Mater.* 2 (2019) 763–776.
- [24] J.-Y. Li, H.-Y. Chen, Y. Jiang, D.-B. Kuang, In situ construction of direct Z-scheme $\text{CsxWO}_3/\text{CsPbBr}_3$ heterojunctions via cosharing Cs atom, *Sol. RRL* 5 (2021) 2100036.
- [25] M.-S. Gui, W.-D. Zhang, Y.-Q. Chang, Y.-X. Yu, One-step hydrothermal preparation strategy for nanostructured $\text{WO}_3/\text{Bi}_2\text{WO}_6$ heterojunction with high visible light photocatalytic activity, *Chem. Eng. J.* 197 (2012) 283–288.
- [26] L. Ding, Y. Ding, F. Bai, G. Chen, S. Zhang, X. Yang, H. Li, X. Wang, In situ growth of $\text{Cs}_3\text{Bi}_2\text{Br}_9$ quantum dots on Bi-MOF nanosheets via cosharing bismuth atoms for CO_2 capture and photocatalytic reduction, *Inorg. Chem.* 62 (2023) 2289–2303.
- [27] X. Lian, J. Zhang, Y. Zhan, Y. Zhang, S. Yang, Z. Chen, Y. Dong, W. Fang, X. Yi, Engineering $\text{BiVO}_4/\text{Bi}_2\text{S}_3$ heterojunction by cosharing bismuth atoms toward boosted photocatalytic Cr(VI) reduction, *J. Hazard. Mater.* 406 (2021), 124705.
- [28] Z. Luo, X. Ye, S. Zhang, S. Xue, C. Yang, Y. Hou, W. Xing, R. Yu, J. Sun, Z. Yu, X. Wang, Unveiling the charge transfer dynamics steered by built-in electric fields in BiOBr photocatalysts, *Nat. Commun.* 13 (2022) 2230.
- [29] J. Deng, D. Xu, J. Zhang, Q. Xu, Y. Yang, Z. Wei, Z. Su, $\text{Cs}_3\text{Bi}_2\text{Br}_9/\text{BiOBr}$ S-scheme heterojunction for selective oxidation of benzylic C–H bonds, *J. Mater. Sci. Technol.* (2023).
- [30] S. Song, Z. Xing, H. Zhao, Z. Li, Z. Wei, Recent advances in bismuth-based photocatalysts: environment and energy applications, *Green. Energy Environ.* (2022).
- [31] W.M. Linhart, S.J. Zelewski, P. Scharoch, F. Dybala, R. Kudrawiec, Nesting-like band gap in bismuth sulfide Bi_2S_3 , *J. Mater. Chem. C* 9 (2021) 13733–13738.
- [32] W.-N. Wang, C.-Y. Zhang, M.-F. Zhang, P. Pei, W. Zhou, Z.-B. Zha, M. Shao, H.-S. Qian, Precisely photothermal controlled releasing of antibacterial agent from Bi_2S_3 hollow microspheres triggered by NIR light for water sterilization, *Chem. Eng. J.* 381 (2020), 122630.
- [33] J.H. Kim, A. Ma, H. Jung, H.Y. Kim, H.R. Choe, Y.H. Kim, K.M. Nam, In situ growth of the Bi_2S_3 nanowire array on the Bi_2MoO_6 film for an improved photoelectrochemical performance, *ACS Omega* 4 (2019) 17359–17365.
- [34] L. Hao, P. Ju, Y. Zhang, C. Sun, K. Dou, D. Liao, X. Zhai, Z. Lu, Novel plate-on-plate hollow structured BiOBr/ Bi_2MoO_6 p-n heterojunctions: In-situ chemical etching preparation and highly improved photocatalytic antibacterial activity, *Sep. Purif. Technol.* 298 (2022), 121666.
- [35] L. Liu, H. Huang, F. Chen, H. Yu, N. Tian, Y. Zhang, T. Zhang, Cooperation of oxygen vacancies and 2D ultrathin structure promoting CO_2 photoreduction performance of $\text{Bi}_4\text{Ti}_3\text{O}_{12}$, *Sci. Bull.* 65 (2020) 934–943.
- [36] Z. Long, G. Zhang, H. Du, J. Zhu, J. Li, Preparation and application of BiOBr- Bi_2S_3 heterojunctions for efficient photocatalytic removal of Cr(VI), *J. Hazard. Mater.* 407 (2021), 124394.
- [37] T. Panda, P. Pachfule, Y. Chen, J. Jiang, R. Banerjee, Amino functionalized zeolitic tetraxlate framework (ZTF) with high capacity for storage of carbon dioxide, *Chem. Commun.* 47 (2011) 2011–2013.
- [38] W. Gu, X. Li, W. Zhang, J. Wang, X. Yin, L. Zhu, Z. Chen, W. Zou, Z. Fu, Y. Lu, Self-limited ion-exchange grown $\text{Bi}_4\text{Fe}_2\text{Ti}_3\text{O}_{18}$ -BiOBr ferroelectric heterostructure and the enhanced photocatalytic oxygen evolution, *Appl. Surf. Sci.* 479 (2019) 137–147.
- [39] F. Liu, S. Zhang, D. Xu, F. Sun, W. Wang, X. Li, W. Yu, X. Dong, G. Liu, H. Yu, Columnar cactus-like 2D/1D BiOBr/ $\text{BiVO}_4\cdot\text{Yb}^{3+}, \text{Er}^{3+}$ heterostructure photocatalyst with ultraviolet-visible-near infrared response for photocatalytic degrading dyes, endocrine disruptors and antibiotics, *J. Alloy. Compd.* 929 (2022), 167330.
- [40] C. Tian, S. Luo, J. She, Y. Qing, N. Yan, Y. Wu, Z. Liu, Cellulose nanofibrils enable flower-like BiOCl for high-performance photocatalysis under visible-light irradiation, *Appl. Surf. Sci.* 464 (2019) 606–615.
- [41] O. Mehranj, N.A. Mir, B.M. Pirzada, S. Sabir, Fabrication of novel $\text{Ag}_3\text{PO}_4/\text{BiOBr}$ heterojunction with high stability and enhanced visible-light-driven photocatalytic activity, *Appl. Surf. Sci.* 332 (2015) 419–429.
- [42] Y. Wu, W. Xu, W. Tang, Z. Wang, Y. Wang, Z. Lv, Y. Zhang, W. Zhong, H.-L. Cai, R. Yang, X.S. Wu, In-situ annealed “M-scheme” MXene-based photocatalyst for enhanced photoelectric performance and highly selective CO_2 photoreduction, *Nano Energy* 90 (2021), 106532.
- [43] S.M. El-Sheikh, A.B. Azzam, R.A. Geioushy, F.M. El Dars, B.A. Salah, Visible-light-driven 3D hierarchical $\text{Bi}_2\text{S}_3/\text{BiOBr}$ hybrid structure for superior photocatalytic Cr(VI) Reduct., *J. Alloy. Compd.* 857 (2021), 157513.
- [44] Y. Li, T. Liu, Z. Cheng, Y. Peng, S. Yang, Y. Zhang, Facile synthesis of high crystallinity and oxygen vacancies rich bismuth oxybromide upconversion nanosheets by air-annealing for UV-Vis-NIR broad spectrum driven Bisphenol A degradation, *Chem. Eng. J.* 421 (2021), 127868.
- [45] Y. Zhang, J. Di, X. Zhu, M. Ji, C. Chen, Y. Liu, L. Li, T. Wei, H. Li, J. Xia, Chemical bonding interface in $\text{Bi}_2\text{Sn}_2\text{O}_7/\text{BiOBr}$ S-scheme heterojunction triggering efficient N_2 photofixation, *Appl. Catal. B* 323 (2023), 122148.
- [46] J. Wu, X. Li, W. Shi, P. Ling, Y. Sun, X. Jiao, S. Gao, L. Liang, J. Xu, W. Yan, C. Wang, Y. Xie, Efficient visible-light-driven CO_2 reduction mediated by defect-engineered BiOBr atomic layers, *Angew. Chem. Int. Ed.* 57 (2018) 8719–8723.
- [47] T. Zhao, Z. Xing, Z. Xiu, Z. Li, P. Chen, Q. Zhu, W. Zhou, Synergistic effect of surface plasmon resonance, Ti^{3+} and oxygen vacancy defects on $\text{Ag}/\text{MoS}_2/\text{TiO}_2$ -x ternary heterojunctions with enhancing photothermal catalysis for low-temperature wastewater degradation, *J. Hazard. Mater.* 364 (2019) 117–124.
- [48] X. Dong, L. Xu, J. Ma, Y. Li, Z. Yin, D. Chen, Q. Wang, J. Han, J. Qiu, Z. Yang, Z. Song, Enhanced interfacial charge transfer and photothermal effect via in-situ construction of atom co-sharing Bi plasmonic/ $\text{Bi}_4\text{O}_5\text{Br}_2$ nanosheet heterojunction towards improved full-spectrum photocatalysis, *Chem. Eng. J.* 459 (2023), 141557.
- [49] Y. Shi, L. Li, Z. Xu, F. Guo, W. Shi, Construction of full solar-spectrum available S-scheme heterojunction for boosted photothermal-assisted photocatalytic H_2 production, *Chem. Eng. J.* 459 (2023), 141549.
- [50] Y. Li, Z. Cheng, L. Yao, S. Yang, Y. Zhang, Boosting NIR-driven photocatalytic activity of $\text{BiOBr}:\text{Yb}^{3+}/\text{Er}^{3+}/\text{Ho}^{3+}$ nanosheets by enhanced green upconversion emissions via energy transfer from Er^{3+} to Ho^{3+} ions, *ACS Sustain. Chem. Eng.* 7 (2019) 18185–18196.
- [51] M. Chahkandi, M. Zargazi, Novel method of square wave voltammetry for deposition of Bi_2S_3 thin film: photocatalytic reduction of hexavalent Cr in single and binary mixtures, *J. Hazard. Mater.* 380 (2019), 120879.
- [52] S. Li, C. Wang, M. Cai, F. Yang, Y. Liu, J. Chen, P. Zhang, X. Li, X. Chen, Facile fabrication of TaON/ Bi_2MoO_6 core-shell S-scheme heterojunction nanofibers for boosting visible-light catalytic levofloxacin degradation and Cr(VI) reduction, *Chem. Eng. J.* 428 (2022), 131158.
- [53] Z. Miao, Q. Wang, Y. Zhang, L. Meng, X. Wang, In situ construction of S-scheme AgBr/BiOBr heterojunction with surface oxygen vacancy for boosting photocatalytic CO_2 reduction with H_2O , *Appl. Catal. B* 301 (2022), 120802.
- [54] X. Ma, Y. Liu, Y. Wang, Z. Jin, $\text{Co}_3\text{O}_4/\text{CeO}_2$ p-n heterojunction construction and application for efficient photocatalytic hydrogen evolution, *Int. J. Hydrog. Energy* 46 (2021) 33809–33822.
- [55] X. Li, B. Kang, F. Dong, Z. Zhang, X. Luo, L. Han, J. Huang, Z. Feng, Z. Chen, J. Xu, B. Peng, Z.L. Wang, Enhanced photocatalytic degradation and $\text{H}_2/\text{H}_2\text{O}_2$ production performance of S-pCN/ $\text{WO}_{2.72}$ S-scheme heterojunction with appropriate surface oxygen vacancies, *Nano Energy* 81 (2021), 105671.
- [56] P. Chen, T. Du, H. Jia, L. Zhou, Q. Yue, H. Wang, Y. Wang, A novel $\text{Bi}_2\text{WO}_6/\text{Si}$ heterostructure photocatalyst with Fermi level shift in valence band realizes efficient reduction of CO_2 under visible light, *Appl. Surf. Sci.* 585 (2022), 152665.
- [57] Q. Xu, S. Wageh, A.A. Al-Ghamdi, X. Li, Design principle of S-scheme heterojunction photocatalyst, *J. Mater. Sci. Technol.* 124 (2022) 171–173.
- [58] H. Li, S. Tao, S. Wan, G. Qiu, Q. Long, J. Yu, S. Cao, S-scheme heterojunction of ZnCdS nanospheres and dibenzothiophene modified graphite carbon nitride for enhanced H_2 production, *Chin. J. Catal.* 46 (2023) 167–176.
- [59] H. Wu, Z. Hu, R. Liang, O.V. Nkwachukwu, O.A. Arotiba, M. Zhou, Novel $\text{Bi}_2\text{Sn}_2\text{O}_7$ quantum dots/ TiO_2 nanotube arrays S-scheme heterojunction for enhanced photoelectrocatalytic degradation of sulfamethazine, *Appl. Catal. B* 321 (2023), 122053.
- [60] M. Tan, Y. Ma, C. Yu, Q. Luan, J. Li, C. Liu, W. Dong, Y. Su, L. Qiao, L. Gao, Q. Lu, Y. Bai, Boosting photocatalytic hydrogen production via interfacial engineering on 2D ultrathin Z-scheme $\text{ZnIn}_2\text{S}_4/\text{g-C}_3\text{N}_4$ heterojunction, *Adv. Funct. Mater.* 32 (2022) 2111740.
- [61] W. Shi, W. Sun, Y. Liu, K. Zhang, H. Sun, X. Lin, Y. Hong, F. Guo, A self-sufficient photo-Fenton system with coupling in-situ production H_2O_2 of ultrathin porous $\text{g-C}_3\text{N}_4$ nanosheets and amorphous FeOOH quantum dots, *J. Hazard. Mater.* 436 (2022), 129141.
- [62] S. Hu, J. Shi, B. Luo, C. Ai, D. Jing, Significantly enhanced photothermal catalytic hydrogen evolution over $\text{Cu}_2\text{O-rGO}/\text{TiO}_2$ composite with full spectrum solar light, *J. Colloid Interface Sci.* 608 (2022) 2058–2065.
- [63] H. Xu, Z. Wu, M. Ding, X. Gao, Microwave-assisted synthesis of flower-like BN/ BiOCl composites for photocatalytic Cr(VI) reduction upon visible-light irradiation, *Mater. Des.* 114 (2017) 129–138.
- [64] Q. Ge, X. Feng, R. Wang, R. Zheng, S. Luo, L. Duan, Y. Ji, J. Lin, H. Chen, Mixed redox-couple-involved chalcopyrite phase CuFeS_2 quantum dots for highly efficient Cr(VI) removal, *Environ. Sci. Technol.* 54 (2020) 8022–8031.